Decoding a complex record of anthropogenic and natural impacts in the Lake of Cavazzo sediments, NE Italy

Alina Polonia [a,*], Sonia Albertazzi [a], Luca Giorgio Bellucci [a], Carla Bonetti [a,b], Jarbas Bonetti [a,b], Giulia Giorgetti [a], Silvia Giuliani [a], Matthias López Correa [a,c], Christoph Mayr [d,e], Laura Peruzza [f], Giuseppe Stanghellini [a], Luca Gasperini [a]

[a] CNR-ISMAR, Via Gobetti 101, I-40129 Bologna, Italy
[b] Laboratório de Oceanografia Costeira, Centro de Ciências Físicas e Matemáticas, Universidade Federal de Santa Catarina, Campus Universitário, CEP 88040-900 Florianópolis, SC, Brazil
[c] GeoZentrum Nordbayern, Friedrich-Alexander Universität Erlangen-Nürnberg, Loewenichstr. 28, D-91054 Erlangen, Germany
[d] Institute of Geography, Friedrich-Alexander Universität Erlangen-Nürnberg, Wetterkreuz 15, 91058 Erlangen, Germany
[e] Dept. Earth and Environmental Sciences, GeoBio-Center, Ludwig-Maximilians-Universität München, Richard-Wagner-Str. 10, 80333 Munich, Germany
[f] Istituto Nazionale di Oceanografia e di Geofisica Sperimentale—OGS, Sgonico, TS, Italy

HIGHLIGHTS

- Multiple stressors, natural and anthropic, affect the equilibrium of the lake.
- The power plant altered the pristine environment.
- The anthropogenic impact favoured the occurrence of sediment lamination.
- Dark laminae higher in S suggest more reducing conditions on the lakefloor.
- AD 1976 earthquakes triggered sediment import via mass transport (seismo-turbidite).

GRAPHICAL ABSTRACT
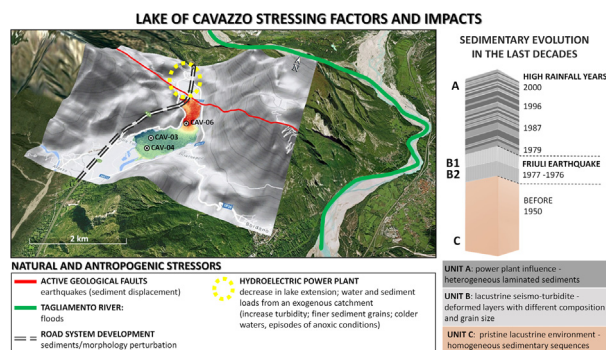
ARTICLE INFO

ABSTRACT

The *Lake of Cavazzo* is a natural, lacustrine basin in the *Friuli-Venezia Giulia* region (NE Italy), which occupies a fluvio-glacial suspended valley of the *Tagliamento* river, at the southern front of the Alpine chain. The lake formed after the melting of major glacial tongues at the end of the Last Glacial Maximum, and has been affected in recent years by natural and anthropogenic events, with economic, cultural and environmental consequences. According to local witnesses, the lake environment has changed dramatically after the 1950s, when the basin was connected to a hydroelectric power plant collecting waters from a wider catchment area, as it served as its final discharge basin.

In this work, based on a densely-spaced grid of high-resolution seismic reflection profiles complemented by sediment cores, we analysed the uppermost lake stratigraphy, highlighting major changes occurring at a decadal scale. Our main purpose is to verify whether and how the lake sediments record the transition from pristine/natural to artificial conditions, as well as the effects of multiple natural impacts including the 1976–77 Friuli earthquake sequence. The results of our analysis suggest varying environmental conditions of the lake after the 1950s indicated by changing sediment mineralogy, increased deposition of allochthonous clastic sediments, and recurrent episodes of anoxic conditions at the lake's floor, likely triggered by hyperpycnal flows derived from the hydroelectric power plant discharges. We also observe that the effects of the 1976–77 seismic sequence

* Corresponding author.
  E-mail address: alina.polonia@cnr.it (A. Polonia).

are recorded in the lake as resedimented levels, likely due to shaking, in situ deformation, landslides, and turbidity currents. Our results stress the importance of lacustrine environments as efficient recorders of anthropogenic and natural events.

1. Introduction

The *Lake of Cavazzo* occupies an area of 1.4 km^2 in the Eastern Alps (Friuli Venezia Region, NE Italy), at an altitude of 195 m a.s.l. (Fig. 1). It was formed as a natural fresh water basin after the Last Glacial Maximum (LGM), when a fluvio-glacial valley carved by glaciers was dammed by end-moraine deposits (Venturini and Discenza, 2010). The bedrock in proximity of the lake shores consists mostly of Triassic-Cretaceous limestones and dolostones, while near the northern and southern shores, outcrops are dominated by Quaternary deposits, including fluvio-glacial sediments (north side) and marshes (south side), dating to the upper Pleistocene (Monegato and Stefani, 2011).

It is located in a seismically active region of the Southern Alps within the Eurasia-Adria collision zone and undergoes about 2 mm yr^{-1} of crustal shortening (Anderlini et al., 2020). Predominant tectonic structures are seismogenic faults, which are considered sources of strong earthquakes reported in the region since Medieval times. The lake's surroundings are characterized by a complex structural setting, with intense deformation and shortening (Zanferrari et al., 2013), under the interference between the west-verging NW-SE Paleogene External Dinarides thrust belt and Neogene-Quaternary Alpine tectonics.

Earthquake catalogues include reports of the most destructive events in the region (Rovida et al., 2020). On May 6, 1976 a M$_L$ 6.4 earthquake struck central Friuli region, destroying villages and causing 977 casualties (Slejko et al., 1999). Focal mechanisms show thrust solutions, on planes gently dipping towards the North (Saraò et al., 2021). The main shock was followed by a renewal of the sequence in September (the strongest ones on September 15, 1976). The main 1976 shocks are proposed to be associated with blind thrusts buried below the Friuli plain (Peruzza et al., 2002; Poli et al., 2002). Seismicity was located eastwards of the Tagliamento river valley (Fig. 1), and it migrated towards the NW in September (Aoudia et al., 2000; Pondrelli et al., 2001). The final phase of seismic activity started on September 16, 1977, with a moderate shock (M$_L$ = 5.2) and its aftershocks located SW of the Cavazzo lake (Suhadolc, 1981). These events are considered as the conclusive phase of the 1976–77 seismic sequence in Friuli.

The most relevant surface effects observed after the May 1976 earthquakes were located at the same latitude of the main event epicenter (Ambraseys, 1976; Govi, 1977; Martinis and Cavallin, 1978) and the lake of Cavazzo might represent a key area for investigating the effects of co-seismic deformation and resedimentation processes since the earthquakes caused rock falls and landslides in the lake's valley (Govi, 1977). After pioneer studies (e.g. Sims, 1975; Doig, 1986; Inouchi et al., 1996), lacustrine paleoseismology became a well-established methodology in determining the frequency of large-magnitude earthquakes (Chapron et al., 1999; Strasser et al., 2006; Moernaut et al., 2014; Van Daele et al., 2020; Moernaut, 2020). The potential contribution of lacustrine seismo-stratigraphy and paleoseismology, successfully applied in the southern Alps (Fanetti et al., 2008; Simmoneau et al., 2013; Gasperini et al., 2020), has never been explored in the Friuli region.

Our work was motivated from the observation that the lake of Cavazzo underwent several natural and anthropogenic impacts in the last decades, such as the construction of a hydroelectric power plant in 1953–1958, a major flood of the Tagliamento river in 1966, the sequence of strong earthquakes in 1976–77, and the construction of the A23 highway viaduct in 1973–1979, that modified part of its catchment area. The Somplago power-plant at the northern lake shore (Fig. 1) is supplied by an artificial channel, which drains the water and sediment discharge into the lake. This channel receives waters from a complex system of artificial and natural sources, the so called Ambiesta hydrographic system, fed by two major artificial basins, the lake of Sauris at an altitude of 977 m, and the Lake of Verzegnis, at an altitude of 493 m. Due to the altitude differences, the waters supplied to the Lake of Cavazzo are several degrees colder than those before the power-plant emplacement (Pironio, 1989). The lake has no permanent natural tributaries, but is fed by seasonally-active streams, and its outflow, to the Leale stream, is constituted by an artificial channel built during the construction of the power-plant. Together with seasonal changes in water temperatures, during heavy precipitation events in the Tagliamento catchment area, the power-plant conveys high-turbidity waters into the lake (Fig. DIB1, Polonia et al., 2021), an occurrence never observed before its emplacement. Several attempts have been made to quantify the total sediment load discharged into the lake by the power-plant. Garzon (2011) estimated a volume of over 7 million m^3 of total sediment discharge since 1956, over 50 times the natural rate; however, none of the estimates has yet been based on sediment cores analysis.

Freshwater ecosystems are particularly vulnerable to environmental changes (Dudgeon et al., 2006; Heino et al., 2021) and investigations have been recently developed to discuss aspects related to climate change, land-use intensification, eutrophication, acidification and water level regulation (Smol, 2019; Han et al., 2020; Saber et al., 2020). However, long-term monitoring programs are inexistent for most lacustrine systems and datasets longer than a few years are rare. Accordingly, it is a difficult task to recognize the nature and extent of ecosystem alterations based exclusively on these limited temporal datasets. In this study, we focus on the decennial environmental evolution provided by the sedimentary record of the Lake of Cavazzo. We describe changes in the lake environment and describe how they are related to the atmospheric, geologic, hydrologic, and anthropogenic compartments. Stressing factors such as episodes of intense precipitation, earthquakes, changes in the sediment load and mineral composition, water level oscillations, river flooding, water cooling, anoxia and man-induced morphological alterations are described based on a multiproxy analytical approach, employing physical, geochemical, and micropaleontological descriptors. The advantage of this strategy is the possibility to recognize the extent (along the time) to which the system has been submitted, to identify eventual fragilities on the overall lake's functionality, and to propose mitigation strategies.

2. Materials and methods

This study is based on the analysis of a densely spaced grid of high-resolution seismic reflection profiles and three sediment cores, collected during a geological/geophysical survey in May 2015.

2.1. Seismic reflection data

The seismic reflection data were collected using a motorboat equipped with a Benthos-Teledyne CHIRP III subbottom profiler, which allowed for acquisition of a closely-spaced grid of profiles (Fig. 2a). Acquisition of the main physical parameters along the water column, including temperature, pressure and conductivity, was carried out from the lake centre, to obtain average sound velocities for travel-times/depth conversions. The highly-repeatable frequency-modulated signal generated by the seismic source, as well as the choice of a constant emission power and receiver gain, led us to estimate the lake-floor reflectivity, and use such parameter as diagnostic of sediment characters and distribution. Data processing was performed using the open package SeisPrho (Gasperini and Stanghellini,
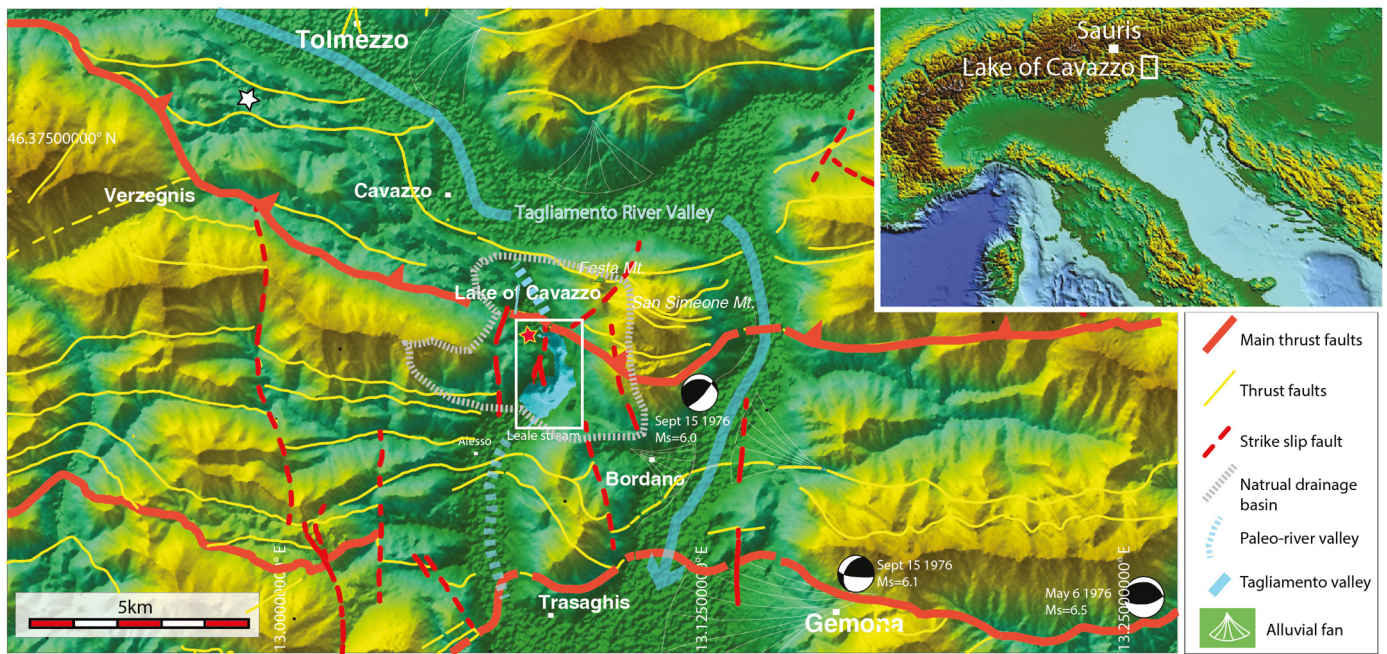
Fig. 1. Location map of the study region within the southern Alpine thrust belt. Main tectonic features modified from the Tectonic map of the Friuli Venezia Region : http://serviziogc. regione.fvg.it/geoserver/web/. Focal mechanisms of the three major earthquakes (May 6, and September 15, 1976) are taken from Aoudia et al. (2000). Red star: location of the Somplago Hydro-electric power plant. White star: Location of 1928 Tolmezzo earthquake (Sandron et al., 2014). White rectangle: part of the artificial post-1950's high-altitude catchment basin. The artificial catchment region is very wide and includes the high-altitude lake of Sauris (inset map).

2009). After filtering and editing of georeferenced points (bathymetry, reflectivity amplitude, etc.), data were gridded using the nearest-neighbour algorithm of the GMT package. In this way, three Netcdf grids were produced including: i) a lake-floor morphobathymetry (Fig. 2b), ii) a lake-floor slope (Fig. 2c), and iii) a lake-floor reflectivity (Fig. 2d). Reflectivity of the sediment-water interface was computed using the method described in Gasperini et al. (2021). We used the average sound speed value of 1446 m s^{-1}, derived by measures in the water column for depth-converting the bathymetry, and a value of 1500 m s^{-1} for a rough estimate of sediment thickness. Correlations between seismic stratigraphy and core-logs were carried out using the Chircor software (Dal Forno and Gasperini, 2009).

2.2. Gravity cores

Cores were collected using a gravity corer with plastic liner of 6 cm diameter preserving the sediment-water interface (Table DIB2 Polonia et al., 2021). Cores CAV-03 (Fig. DIB3 Polonia et al., 2021), CAV-04 and CAV-06 were sampled at 25, 15 and 35 m water depth respectively.

2.2.1. Physical analyses

The cores were studied with different methods, including visual logs and texture/sedimentary features analyses, carried out combining high-resolution colour photos and computed tomography to define main stratigraphic levels. Each core was subsequently sampled at 1 cm interval for grain size analysis, following clinoforms where noticeable. Grain size was determined using a Malvern Mastersizer 3000 analyser and laser-scattering spectra have been processed using the multiple sample analysis function in the Excel worksheet GRADISTAT. Grain-size analysis accounts for all particles included in the sample and are reported on the Wentworth scale (Wentworth, 1922).

Cores CAV-04 and -06 were scanned by a medical Core Axial Tomography scan system, under an X-ray energy of 120 kV and pitch of 0.3. The final images (CAT scan) have a voxel size of $0.5 \times 0.5 \times 1.0$ mm^3 with slice thickness of 1 mm. The intensity of the transmitted X-ray beams is expressed as Hounsfield Unit (HU), which follows the relation:

$HU = (\mu m - \mu_w) / (\mu_w) \times 1000$ where μ_w is the linear attenuation coefficient of the water, and HU depends on X-ray absorption properties of the material (m). High-resolution magnetic susceptibility (MS) logs were acquired with a Bartington MS2 system, equipped with a 100 mm loop sensor at sampling interval of 0.5 cm.

2.2.2. Geochemical and mineralogical proxies

2.2.2.1. XRF-scanning.
Geochemical data of cores CAV-04 and CAV-06 were collected with an Avaatech XRF-CS at ISMAR CNR-Bologna, to estimate the elementary properties of lake sediments and characterize the variations of major elements. The core scanner uses an intense non-destructive X-ray beam that irradiates the sample to detect the energy of fluorescent radiation in order to provide relative level of elemental profiles. It represents a semi-quantitative measurement of elemental variations within the sediments. Continuous elemental variations were obtained at 2 mm scanning resolution during three runs. The first with 10 s exposure time, 10 kV, 400 μA for Al, S, Ca, Ti, and Fe; the second with 20 s exposure time, 30 kV, 400 μA for Zn, Sr, Zr, and Pb. The XRF core scanner results are expressed as peak intensities in counts per second (cps). For a correct use of XRF data, a normalization by means of the ratio with a second element is strongly suggested (Hennekam and De Lange, 2012). Since ED-XRF are performed on wet sediment, the presence of water absorbs X-ray energy affecting preferentially light elements with weak florescence energies and for this reason, Hennekam and De Lange (2012) suggest normalization with Ti. Instrumental limit of detection (ILD) varies with measuring time and element. Comparison of scanning counts with absolute concentrations (Huang et al., 2016) show that for those elements with relatively high concentrations or high detectability, the correlation coefficients are higher than 0.90 for all exposure times. In contrast, for the low detectability or low concentration elements, the correlation coefficients are relatively low, and improve little with increased exposure time. Detection limits are related to atomic weight, and on the chemical composition of the matrix. Reported values for Al are MacDonald et al., 2000 ppm and for Pb are 10 ppm (Richter et al., 2006).
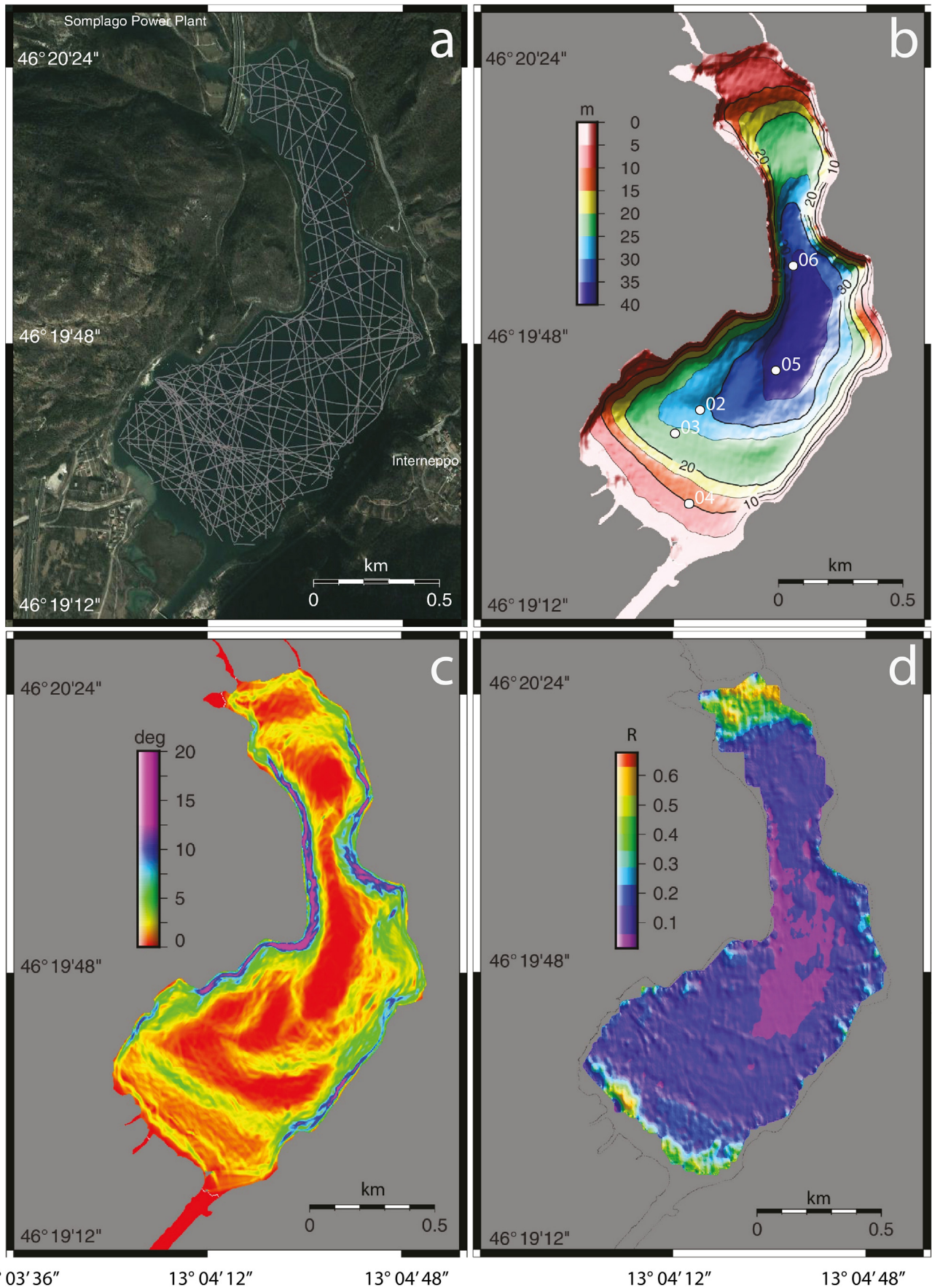
Fig. 2. Lake of Cavazzo region. a) Location map of the acquired seismic reflection data; b) bathymetric map with the location of gravity cores acquired in 2015; c) lake-floor slope: d) lake-floor reflectivity.

2.2.2.2. Bulk sediment mineralogy with x-ray diffractometry (XRD). Mineralogical data were obtained by X-ray Powder Diffraction (XRPD) using a GNR APD2000PRO diffractometer equipped with a secondary graphite monochromator using CuKα radiation (power supply 40 kV/40 mA, 1° divergence and scatter slits, 0.2 mm receiving slit, 0.02° (2θ step size and counting time of 3 s/step, data collection scan 5–65°2θ). We analysed 12 key layers, 5 from core CAV-04 (4, 16, 18, 22, 50 cm) and 7 from core CAV-06 (24, 41, 45, 48, 54, 58, 63 cm).

Before mineralogical analysis, samples were dried at 50 °C and ground in an agate mortar to a very fine powder. Powder samples were filled in a side-entry aluminium holder in order to obtain a quasi-random orientation. Mineralogical parameters were determined from the XRD patterns by the MATCH! analysis software and identification of minerals was based on comparison with PDF-2 reference data from the ICDD (*International Centre Diffraction Data*). A semi-quantitative analysis (statistical error about 10–20%) of minerals identified by XRPD was obtained by a normative re-calculation based on the chemical analysis and Rietveld method.

2.2.2.3. Organic matter: contents and stable isotope. Total carbon (TC) and total nitrogen (TN) were performed on selected homogenized sediments and determined using a *FISONS NA2000* elemental analyser coupled to a *Finnigan Delta Plus* mass spectrometer via a *CONFLO* interface. For measurement of content (TOC) and stable isotope ratios ($\delta^{13}C_{org}$) of total organic carbon, sediments were acidified (HCl, 1.5 M) to remove carbonates. TOC and TN contents are reported as percent of dry weight (wt%). C/N was calculated as molar ratio between TOC and TN (14/12*wt% TOC/wt% TN). The accuracy of element contents, calculated using an atropine standard, is ±0.61 and ±0.11% for carbon and nitrogen, respectively, while precision is 0.07 and 0.01% (1 std. dev.) Accuracy for $\delta^{13}C$ and $\delta^{15}N$ was ± 0.20‰ and ±0.13‰ while precision is better than 0.2‰ (1 std. dev.)

2.2.2.4. Carbonates: characterization and stable isotopes. Samples for characterization of carbonates came from selected depths (2, 11, 21, 39, 42, 50, 52 cm) in core CAV-06. Dried sediment was powdered in an agate mortar and 0.25 μg of this homogenized material was used for $\delta^{13}C_{carb}$ and $\delta^{18}O_{carb}$ analyses of the bulk carbonate fraction. Further 0.25 g of the dry bulk sediment was embedded under vacuum in epoxy resin and polished for optical microscopic documentation and investigation with a Scanning-Electron-Microscope. Light microscopy of polished surfaces (800 grit) was carried out on a ZEISS AxioVision. Seven polished blocks with epoxy-embedded sediment were carbon-coated with a BALTEC MED020 system and thereafter examined with a VEGA-TESCAN Scanning-Electron-Microscope in secondary electron and back-scattered electron modes (SE/BSE) at 20 kV, 9 PC with a typical working distance of 15 mm. Grain sizes and shapes were screened, and BSE-intensities were used to distinguish organic debris from mineral grains.

For carbonate isotope analyses, powdered sediment samples were reacted with 100% phosphoric acid at 70 °C using a Gasbench II connected to a ThermoFisher Delta V Plus mass spectrometer to obtain carbon ($\delta^{13}C_{carb}$) and oxygen ($\delta^{18}O_{carb}$) isotope ratios. $\delta^{13}C_{carb}$ and $\delta^{18}O_{carb}$ values are reported in ‰ relative to V-PDB. International standards (NBS19 and IAEA CO9 for carbon and NBS19 and NBS18 for oxygen were used for calibration and provided a reproducibility for $\delta^{13}C_{carb}$ and $\delta^{18}O_{carb}$ of ±0.07‰ and ±0.05‰ (1 std. dev.), respectively. Bulk sediment contained varying proportions of calcite and dolomite, which has not been accounted for since these isotopic effects were minor compared to observed isotope variations.

2.2.3. Biological proxies: micropaleontology and sediment component analyses

51 samples were selected for biofacies analyses using visual inspection and identification of biogenic components under a stereomicroscope. All samples were stored in an oven with temperatures of 50 °C for 24 h and subsequently weighed. After being left soaking for 24 h into demineralized water, the samples were then wet sieved (mesh size of 63 μm). The residual of all samples was finally filtered and dried at 50 °C. A qualitative description has been carried out including occurrence and nature of carbonate clasts, plant remains (generic vegetal frustules, wood fragments, leaf fragments, algae fragments, oospores, gyrogonites), and benthic thanatocoenoses (shell fragments, bivalve, gastropods, ostracod). Ostracods were classified to genus or, where possible, to species levels based on Henderson (2002) and Pieri et al. (2009). Gastropod shells and opercula were identified through the work of Benantelli et al. (2011). SEM (Scanning Electron Microscope) observations were carried out for detailed analysis of main accessory components selected under the stereomicroscope. Images of interesting elements were collected, such as benthic macrophyte rests, oospores and carbonate clasts (Fig. DIB12 Polonia et al., 2021). On these latter, elemental geochemical analyses were also carried out using an X-ray EDS spectrometer to determine their composition.

2.2.4. ^{210}Pb and ^{137}Cs age model

Sediment chronology of cores CAV-04 and CAV-06 was carried out using ^{210}Pb and ^{137}Cs radioisotopes. ^{210}Pb activities were obtained by measuring its daughter product ^{210}Po assuming secular equilibrium between the two isotopes. Supported ^{210}Pb activities were obtained from the constant values at depth in the cores. For ^{137}Cs determination, freeze-dried sediments were put in standard vessels of suitable geometries and gamma counted (Bellucci et al., 2007).

2.2.5. Statistical analysis of sediment composition

Linear discriminant analysis was run on z-value transformed data in order to find out a linear combination of 12 variables (grain size and XRF-based geochemical features) that could be used to statistically discriminate the predefined lithological units in each core. To avoid the issues of multicollinearity, the input variables were selected considering their correlation coefficients. Statistically significant differences (adopting alpha = 0.05) among the discriminated groups, regarding each variable, were verified by applying Kruskal-Wallis test. The predicted classes obtained by LDA were then used to "downscale" the continuous description of the core log and XRF-CS datasets to a 1 cm-scale resolution (equal to the grain size acquisition interval), in an approach similar to the one adopted by Henares et al. (2019). Since the sampling resolution of the organic geochemical data was irregular and coarser than 1 cm, these variables were not included in the LDA. Notwithstanding, a multiple correlation analysis based on Spearman rank order coefficient was carried out among them and the scores from the first two discriminant axis as a strategy to match these two datasets with different vertical resolutions. An analogous methodological approach was previously applied by Braun et al. (2013). K-means clustering algorithm was applied to identify similar geochemical patterns through the unit A of the core CAV-06 as well as to evaluate the XRF data potential in the laminae geochemical characterization. The number of clusters (k = 3) was chosen based on the best clustering scheme from a compilation of different indices processed by the NbClust R Package, as proposed by Malika et al. (2014). The statistical tests and plots were performed using the softwares PAST (PAleontological STatistics) v 3.25 (Hammer et al., 2001) and R (R Core Team, 2020).

3. Results and interpretation

3.1. Morphology and seismic stratigraphy

The bathymetric map in Fig. 2b shows that the lake is extending in N-S direction for about 2.5 km and displays maximum water depths of around 38 m in its narrower part, close to its centre.

In the southern sector, the slope map (Fig. 2c) highlights the presence of alternating steps and flats, the larger delimiting a southern shelf occupied by aquatic plants, as shown in the chirp-sonar profiles (Fig. 3e). The lake morphology resembles that of a glacially-carved

fluvial valley, and irregularities in the lake floor are due to the presence of alluvial fans from tributaries and debris along the steep flanks.

The reflectivity map (Fig. 2d) shows maximum values in the northern and southern shelves, increasing close to the shores. This is probably due to the presence of coarser deposits and/or roots of aquatic plants. Lower reflectivity values characterize the lake depocenter, where finer-grained deposits are probably accumulating.

The sedimentary sequence of the lake is hardly penetrated by the chirp-sonar signal in most sectors (Fig. 3) due to two main factors: i) coarse grained sediments, close to the lake shores; and ii) widespread presence of gas in the sediments, most probably of biogenic origin, which hamper penetration of the seismic signal. Best penetration is reached in the southern sector, where seismic images show a prominent unconformity separating two units (U1 and U2, Fig. 3a) with different acoustic facies. The upper U1 shows alternating transparent and finely laminated sediment packets, while U2, the lower, shows lateral variations and less continuous seismic reflectors. Acoustic windows are locally present in different sectors of the lake, suggesting a rather homogeneous stratigraphy not visible because of gas bearing sediments (Fig. 3b). The southern shelf is entirely occupied by an up to 10 m thick sediment wedge (Fig. 3c). The base of the wedge is constituted by a sharp, sub-horizontal unconformity H (Fig. 3c and e, stratigraphically lower than that separating units U1 and U2 in Fig. 3a and possibly related to fluvio-glacial processes) overlaying
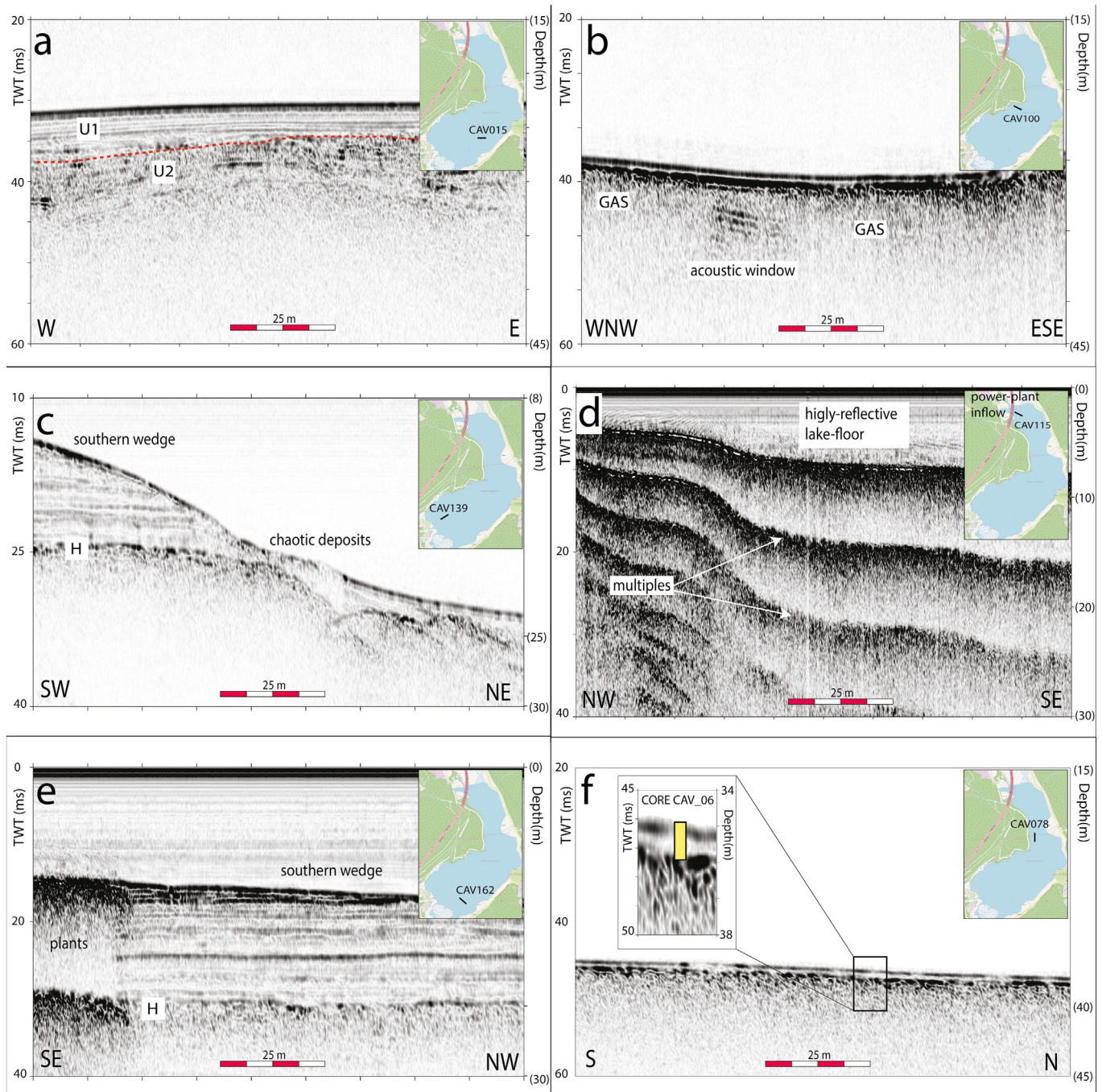

Fig. 3. Seismic reflection images from different sectors of the Lake of Cavazzo representative of different geological processes. a) Profile CAV015 collected in the SE sector showing a sharp unconformity between two different units characterized by different seismic facies. b) The presence of gas in the lake's sediments affect penetration of the seismic signal. c) The southern sector of the lake hosts a thick sediment wedge bounded at its base by a sub-horizontal unconformity; chaotic deposits are observed at the front of the wedge. d) Highly-reflective lake floor found in the northern sector close to the power-plant discharge.

an acoustic basement not penetrated by the seismic waves. This southern wedge is well layered and it appears affected by erosion while its front shows signs of gravitational instability, indicated by the presence of chaotic deposits, over which recent sediments deposited in deeper regions overlap (Fig. 3c). The lake depocenter and the northern sector are characterized by low signal penetration, if we exclude a relatively thin veneer of transparent deposits (Fig. 3f).

3.2. Sedimentary record from gravity cores

Based on multi-proxy analyses of the gravity cores, three main sedimentary units, which show different sediment colour, structure, geochemistry and grain size were identified (Figs. 4–5). From top to bottom, they are named Units A, B, and C.

An uppermost muddy silt Unit A is present at the top of each core. It is characterized by mm- or cm-thick, sub-horizontal light and dark brown laminations. The thickness of this unit is variable: 36, 20 and 40 cm in cores CAV-03 (Fig. DIB3 Polonia et al., 2021), CAV-04 (Fig. 4), and CAV-06 (Fig. 5) respectively. CT scan images show that laminations are present throughout Unit A, showing alternating white and dark sediment bands characterized by a different response in CT scan (Fig. 4). If we consider the thickest dark laminae in core CAV-04 (3–4 cm in Fig. 4), we see that XRF data suggest that it is associated with a decrease in Ca, Zr, Al, Fe and Ti and an increase in Sr and S. In core CAV-06, where more data are available, the dark laminae correspond to minimum values of $CaCO_3$, higher values of TOC and less negative $\delta^{13}C_{org}$.

Unit B does not show internal laminations, at least in its basal part, and is characterized by an increased grain size up to medium sand associated with peaks in MS only in core CAV-04 and varying sediment structure. In core CAV-03 it is represented by "spongy" sediments, very dark in colour associated with increased grain size and sand content up to 20% (Fig. DIB3 Polonia et al., 2021). In core CAV-04, Unit B is 8 cm thick, shows an irregular basal scour and its sand content is up to 65% (Fig. 4). It can be divided into two different sediment packets based on geochemical variations and sedimentological patterns: the lowermost Subunit B2 lacks internal structures and shows the presence of round clasts and a lens of different lithology included in the sandy matrix particularly evident on CT scan images. Subunit B1 shows enrichments in Sr, Zr, Ti, Rb and Zn and in its upper part millimetric laminations are visible on CT scan images. In core CAV-06 Unit B has its maximum thickness of about 20 cm and shows a very complex internal structure and two different Subunits (Fig. 5). The lower Subunit B2 is represented by a very dark basal sediment packet marked by an increase in sand up to 22%. This layer is overlain by light brown sediments bounded at their top by a millimetric coarser level very reflective on the CT scan images (Fig. 5). The uppermost Subunit B1 shows a composite structure made by three distinct sediment packets. At the very base, a porous dark brown oblique lens corresponding to a minimum in $CaCO_3$ is included in a light brown and finer matrix. In the middle part of Subunit B1, sediments are characterized by an alternation of light and dark brown layers. A prominent sand-rich layer of light brown sediments marks the topmost part of the Subunit B1 (Fig. 5). CT scan images provide clues on the existence of two sediment layers with very high reflectivity. The lowermost consists of millimetric sediment laminae at about 54 cm at the top of Subunit B2; the uppermost high reflectivity layer (between 40 and 44 cm), has an irregular geometry, corresponds to a peak in $CaCO_3$ and geochemical anomalies (Ca/Ti, Zr/Ti) and marks the top of Subunit B1.

The lowermost light brown, more compacted sandy-silt Unit C, is present only in core CAV-04 where it is 25 cm thick. XRF data in core CAV-04, show that the top of Unit C is characterized by a sharp change in sediment geochemistry. Sediments above Unit C show higher Al, Ti, Fe, Sr, S, Zr, Zn and Pb elemental levels while sediments belonging to Unit C are richer in Ca.

Unit B shows transitional geochemical composition showing a progressive increase in alumino-silicates, Fe, heavy metals and S. It marks also a change in grain size, since cores CAV-03 and CAV-04 show an increase in clay in Unit A while below Unit B clay is not present in core CAV-04 which penetrated deeper in the lacustrine sediments. Unit A shows also relative enrichments in Zn, Pb and S (Fig. 4). Correlations between cores and seismic reflection profiles suggest that only sediments from seismostratigraphic Unit U1 were reached by our sampling, while direct stratigraphic information about the U1–U2 unconformity is still lacking.

3.2.1. Overall sediment composition in core CAV-06

Under the optical microscope the visual aspect (Fig. DIB4 Polonia et al., 2021) of samples taken from the three units of core CAV-06 is very similar, with sub-millimetre sized light-coloured angular mineral grains floating in a greyish-beige fine matrix. Additionally, all samples comprise dark components with irregular to elongated shapes interpreted as phytodetritus. All samples where easy to pulverize in a mortar, except for the horizon at −42 cm, which comprised hard-whitish angular calcite grains of up to millimetre size. These properties are in line with the bulk carbonate content, which is overall between 50 and 60% but reaches a peak at −42 cm with ~85% (Tab. DIB5 Polonia et al., 2021). Dark units contain with ~50% less bulk carbonate than the light units. Under the optical microscope the sample taken at −42 cm appears as an essentially matrix-free carbonate sand with millimetre-sized angular grains that range typically between 0.1 and 1.5 mm and show a grain-to-grain contact. No rounded mineral components have been found in any of the seven samples.

3.2.2. SEM-results

The general similarity observed with the optical microscope (Fig. DIB4 Polonia et al., 2021) holds up under the SEM (Fig. DIB6 Polonia et al., 2021), for layers at 2, 11, 21, 39, 50 and 52 cm, while the event bed at −42 cm is markedly different (Figs. DIB4E, DIB6E Polonia et al., 2021). Under the SEM dolomite grains appear as light grey, calcite grains as white and phytodetritus as black in BSE images (Figs. DIB6, DIB7 Polonia et al., 2021). All mineral grains observed throughout these levels are angular in shape, irrespective of their size. While the largest grains, that were visible in optical microscopy, attain up to about 50 μm in length, also the grains within the matrix show exclusively angular outlines. Interestingly, the finer grains (4–10 μm) of the matrix comprise the same component triplet with dolomite, calcite and phytodetritus (Figs. DIB6, DIB7A Polonia et al., 2021), bound by the clay-mineral illite. Phytodetritus content is highest in macroscopically dark core units at 21, 39 and 50 cm. The sample at 39 cm contains a brachiopod fossil (Fig. DIB7A Polonia et al., 2021) and hints to the erosion of marine carbonates in the small catchment area of the lake, and hence to a detrital origin. The event bed at 42 cm is dominated by angular calcite grains that are in direct contact and a matrix is mostly lacking. In some parts of the sample these much larger calcite grains are embedded in a sediment that resembles those of the other six samples (Fig. DIB7B Polonia et al., 2021). This unit comprises also rounded sediment-intraclasts (Fig. DIB7B Polonia et al., 2021) resembling the other six investigated levels, and clearly votes for a reworking of deeper lake sediments.

3.2.3. X-ray diffraction analysis

X-ray diffraction analyses show that main components are calcite, dolomite, illite, chlorite, quartz, plagioclase and amphibole but their occurrence varies throughout the cores and show significant differences in the three sediment units (Fig. DIB8 Polonia et al., 2021).

In core CAV-04, calcite and dolomite together represent 90% of the minerals in Unit C while their abundance is reduced to about 50% in the uppermost Unit A where mica components (illite and chlorite), plagioclase and gypsum are more abundant (up to 29%, 3% and 3% respectively). Unit B shows intermediate mineralogical characteristics with calcite and dolomite (60–78%) along with micas (7–27%) being the main components. Gypsum and quartz increase in Unit B but they show maximum percentages in Unit A.
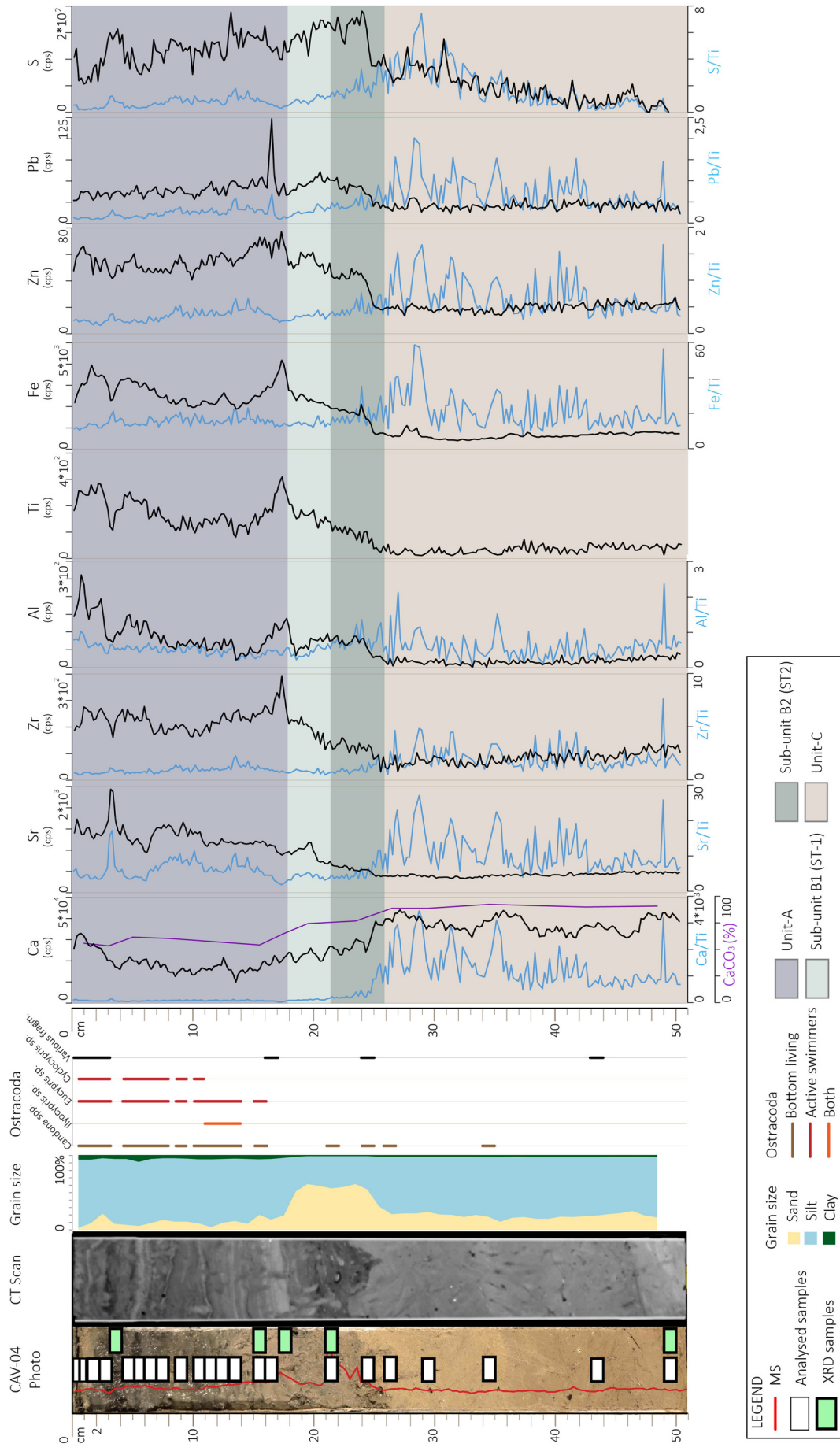
Fig. 4. Log of core CAV-04. From left to right: photograph with magnetic susceptibility in red, CAT scan, grain size, ostracoda distribution, XRF data and subdivision in individual ST units (A, B1, B2 and C) identified by different colours. The XRF core scanner results are expressed as peak intensities by counts per second (cps). Both semi-quantitative elemental levels (cps) without normalization (black curves) and element ratios normalized on Ti (blue curves) are shown.
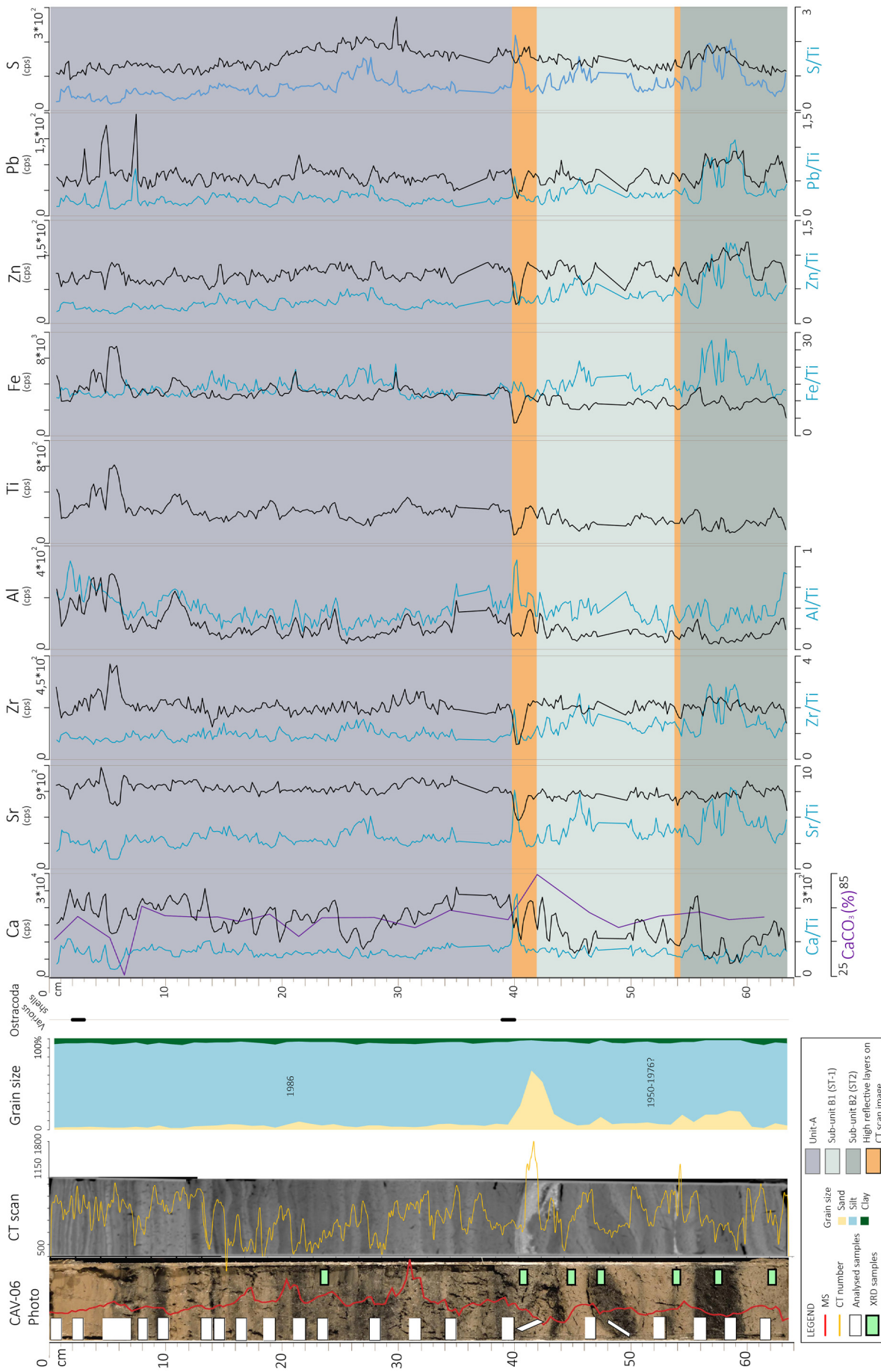
Fig. 5. Log of core CAV-06. From left to right: photograph with magnetic susceptibility in red, CAT scan, grain size, ostracoda distribution, XRF data and subdivision in individual ST units (A, B1, B2 and C) identified by different colours. The XRF core scanner results are expressed as peak intensities by counts per second (cps). Both semi-quantitative elemental levels (cps) without normalization (black curves) and element ratios normalized on Ti (blue curves) are shown.

In core CAV-06 calcite plus dolomite contents in Unit A is around 55% and the other main components are micas (illite 18% and chlorite 6%) and quartz. A significant increase in calcite content characterizes samples at 41 and 45 cm depth, at the upper boundary of Subunit B1, where the high reflective layer was observed in the CT scan images (Fig. 5). This interval is constituted by 66% of calcite (Fig. DIB8 Polonia et al., 2021) more than twice relative to the other samples. The relative mineral abundance derived from Rietveld-analyzes shows an abundance sequence that remains unchanged across most of the core CAV-06 (Fig. DIB9 Polonia et al., 2021). Average compositions and variations (1 stdv.) are: Gypsum 1.0 ± 1.2%, Plagioclase 2.6 ± 1.1%, Amphibole 3.1 ± 0.9%, Chloride 5.1 ± 1.1%, Quartz 9.7 ± 3.0%, Illite 15.1 ± 4.7%, Calcite 25.6 ± 2.1%, Dolomite 31.2 ± 1.8%. Calcite is more prevalent than Dolomite at core depths 45 and 41 cm with 66% to 16% and 50% to 25%, respectively (Fig. DIB9A Polonia et al., 2021). This clear reversal contrasts with the rest of the core and hints to an import of the calcite grains from a shallower depth into the deeper lake basin, which is further supported by their larger grainsize. While calcite dominates at 45 and 41 cm, the other minerals appear to decrease (Fig. DIB9A Polonia et al., 2021), once calcite is removed, it becomes evident that also dolomite is relatively enriched at these horizons and also at 54 cm (Fig. DIB9B Polonia et al., 2021). The typical dolomite prevalence over calcite in Units A and C of core CAV-06 (Fig. DIB9 Polonia et al., 2021), contrasts with the prevalence of calcite over dolomite in the shallow water core CAV-04 (Fig. DIB10 Polonia et al., 2021). As input-component dolomite appears to have a bias towards finer grain-sizes, compared to the more competent calcite grains. Calcite dominates hence in the deposition at shallower near-shore sites, while fine dolomite and fine calcite grains are transported further towards the deeper lake centre (Fig. DIB11 Polonia et al., 2021).

3.2.4. Carbonate stable isotopes

Bulk sediment stable isotope compositions in core CAV-06 are listed in Table DIB5 (Polonia et al., 2021). Oxygen isotopes ($\delta^{18}O_{carb}$) vary between 1.4 and 2.0‰ VPDB, without clear trends across the core and without influence from drastically changing mineralogical proportions of dolomite vs. calcite across the event beds. Carbon isotopes ($\delta^{13}C_{carb}$) vary between −5.5 and −3.1‰ VPDB and with no ties to lithology.

3.2.5. Biogenic components

All samples contain vegetal rests, mostly bark fragments and macrophyte algae (*Chara* sp.) and other elements correlated to macrophyte biological activity, such as oospores and $CaCO_3$ fragments. Core CAV-04 shows the larger diversity in vegetal remains. Between 0 and 11 cm (Unit A) abundant benthic macrophyte remains are found. Wood fragments are more abundant between 22 and 50 cm (Units B and C). In Unit B we observe a fining-upward trend of wood particles with centimetric fragments close to its irregular base. Benthic fauna remnants include gastropods and ostracods valves (Fig. DIB12 Polonia et al., 2021). In core CAV-03, ostracod shell fragments belonging to the genus *Candona* are present. They are rare in Unit A, while Unit B is characterized by relatively abundant fragments and preserved valves. Core CAV-04 displays the highest diversity of the freshwater thanatocoenosis: well-preserved valves are ubiquitous in Units A and B. In the darker, upper part of Unit A, valves of the nektonic genera *Eucypris* and *Cyclocypris* (Henderson, 2002) and the taxon *Candona* (Henderson, 2002) are present together with *Ilyocypris* sp. (mainly benthic, according to Henderson). In Unit C, poorly preserved valves of *Candona* spp. occurred rarely. Core CAV-06 shows a discontinuous ostracod distribution in the sediment units, since very rare valves of *Candona candida* are found only in the uppermost and lowermost parts of Unit A. Within the three units of core CAV-04, mollusk shells, shell-fragments and opercula are present, particularly of gastropods (*Bithynia* sp.) typical of slowly flowing freshwaters (Benantelli et al., 2011).

3.3. Age model and deposition rates

3.3.1. Laminae counting

The topmost Unit A in core CAV-06 shows very well-developed sediment laminae. Assuming that laminae formation relates to seasonal variations of lacustrine sedimentary processes, the succession of one light and one dark level constitutes an interval corresponding to one year. Based on the colour and the number of the laminae, we carried out a chronological reconstruction for sediment deposition. In conjunction with laminae counting, we used rain data (www.meteo.fvg.it) and ^{137}Cs data (see next section) in order to validate our model. The laminae count on core CAV-06 suggests that the depth of 41 cm may correspond to the year 1977. Our reconstruction is confirmed by ^{137}Cs data and by the correlation between ages deduced through laminae counting and rainfall data: more rainy periods (www.meteo.fvg.it) correspond to the thickest laminae in our layer-counting model (Figs. 6c and DIB13 Polonia et al., 2021).

3.3.2. Radiometric dating

^{210}Pb activities in core CAV-04 define a profile that is ascribable to a constant and undisturbed sedimentation only in the uppermost part of the core, from 0 to 18 cm depth (Fig. 6a). Below 18 cm depth the ^{210}Pb profile does not follow a typical decreasing pattern, therefore dating models cannot be applied there. Between 0 and 18 cm depth, the Constant Flux – Constant Sedimentation (CF-CS) model by Appleby and Oldfield (1992) provides a sedimentation rate of 0.4 cm yr^{-1}, assuming as background value the activity measured at 26.5 cm depth (25 Bq kg^{-1}, in accordance with values for supported ^{210}Pb measured in Italy; Bellucci et al., 2012). The sedimentation rate calculated through ^{210}Pb values is reduced to 0.3 cm yr^{-1} when considering the ^{137}Cs peak between 8 and 9 cm depth as a marker of the Chernobyl accident's fallout in 1986 (Fig. 6a). An average sedimentation rate of 0.35 cm yr^{-1} (that includes all possible associated uncertainties relative to sampling, measurement and post-depositional ^{137}Cs migration along the core profile) can then be assumed for the layer from 0 to 10 cm depth in this core. ^{137}Cs activity is completely absent below 26 cm depth, therefore this depth can be associated to the early 1950s, when ^{137}Cs started to be produced through nuclear weapon testing (Bjerregaard and Andersen, 2007). The sandy layer between 18 and 26 cm depth shows a relatively small peak of ^{210}Pb, but, as already stated, values tend to further increase with depth (Fig. 6a), thus preventing any reliable age modelling for this part of the core.

^{210}Pb activities in core CAV-06 are useless for dating purposes because values fluctuate around 60 Bq kg^{-1} throughout the entire core length and do not follow an exponential decreasing trend (Fig. 6b). Such effects could have resulted from the contribution of different inputs or by the redeposition of sediments that were originally deposited elsewhere in the lake or in the catchment area of the power plant. However (and despite the low vertical resolution), ^{137}Cs shows a clear peak at 21 cm depth that can be ascribed to the Chernobyl fallout in 1986 and this chronological marker allows the calculation of a sedimentation rate of 0.7 cm yr^{-1} down to this point. ^{137}Cs is still detected at the core bottom, in accordance with varve counting that defines a depositional timeframe for Unit A starting from the end of 70's.

3.4. Statistical analysis of the sediment cores data

The LDA confirms the differentiation among the described units throughout core CAV-04 and CAV-06. In both cores, the two first discriminants were enough to separate these units, as shown in Fig. 7. A comparison of the "a posteriori" predicted group membership with the "a priori" ones shows that 98% of the cases are correctly classified for CAV-04 and 95.2% for CAV-06. Some of the misclassified cases are placed close to boundaries between events, explaining the statistical discordance due to transitional depositional conditions. Sediment Units can be statistically characterized by differences in their
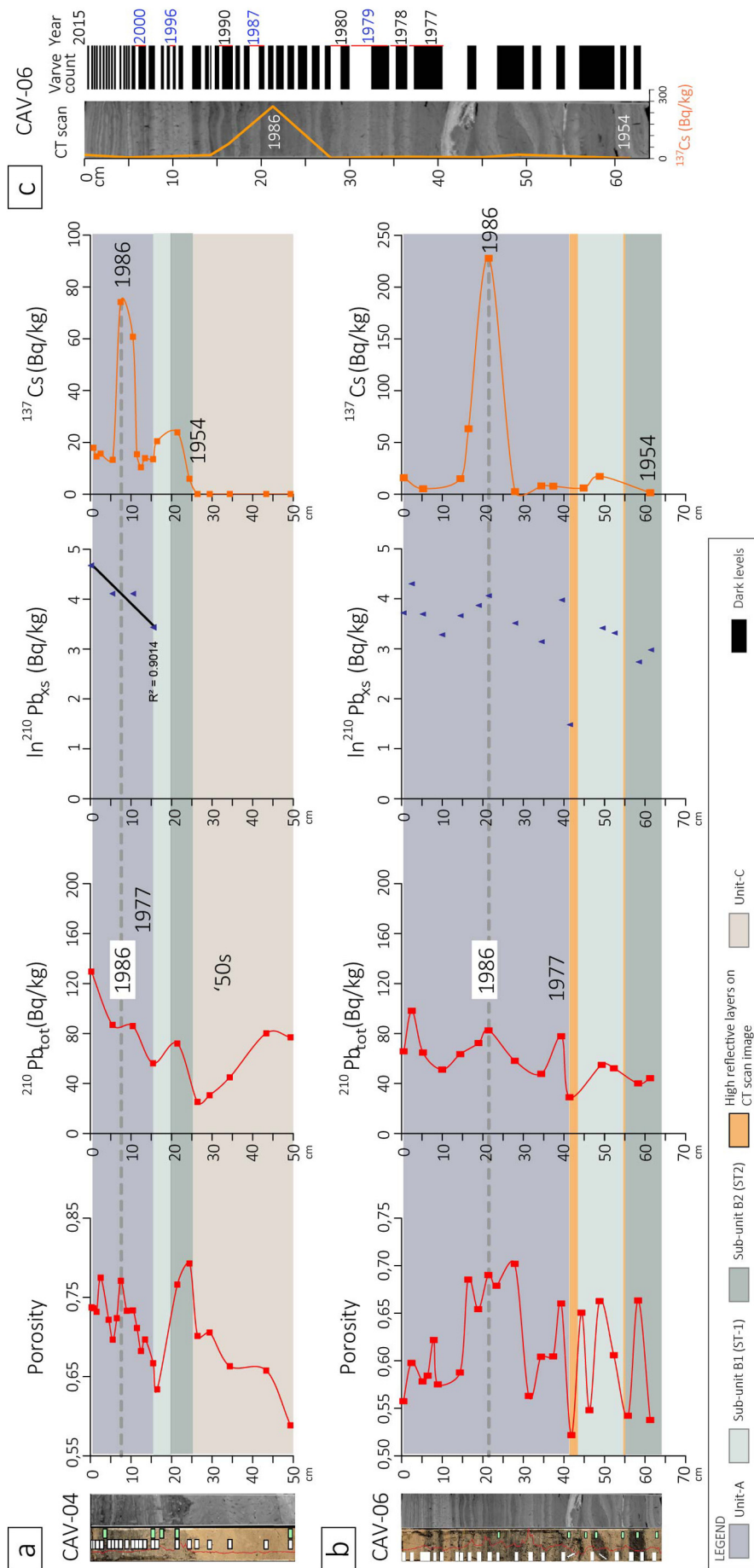
Fig. 6. Profiles of porosity, total ^{210}Pb, $\ln^{210}Pb_{xs}$ and ^{137}Cs in core CAV-04 (a) and CAV-06 (b). $^{210}Pb_{xs}$ is calculated by subtracting the background ^{210}Pb from total activities (see text). Dashed lines enclose the sandy layers observed in both cores. Chronological benchmarks (as years of deposition) are shown on the right side. c) Chronological reconstruction based on varve count. The succession of one light and dark levels constitutes the interval corresponding to a year. In conjunction with laminae counting we use rain data for the lake of Cavazzo region (www.meteo.fvg.it, n.d) in order to validate our model. The thickest laminae correlate well with main atmospheric events, which should have produced an increase in sediment discharge within the lake. The varve count on core CAV-06 suggests that the depth of 41 cm may correspond to the year 1977. This is confirmed by the good correlation between our ages and rainfall data: the more rainy periods (1979, 1987, 1996 and 2000 www.meteo.fvg.it) correspond to the thickest laminae in our varve model.
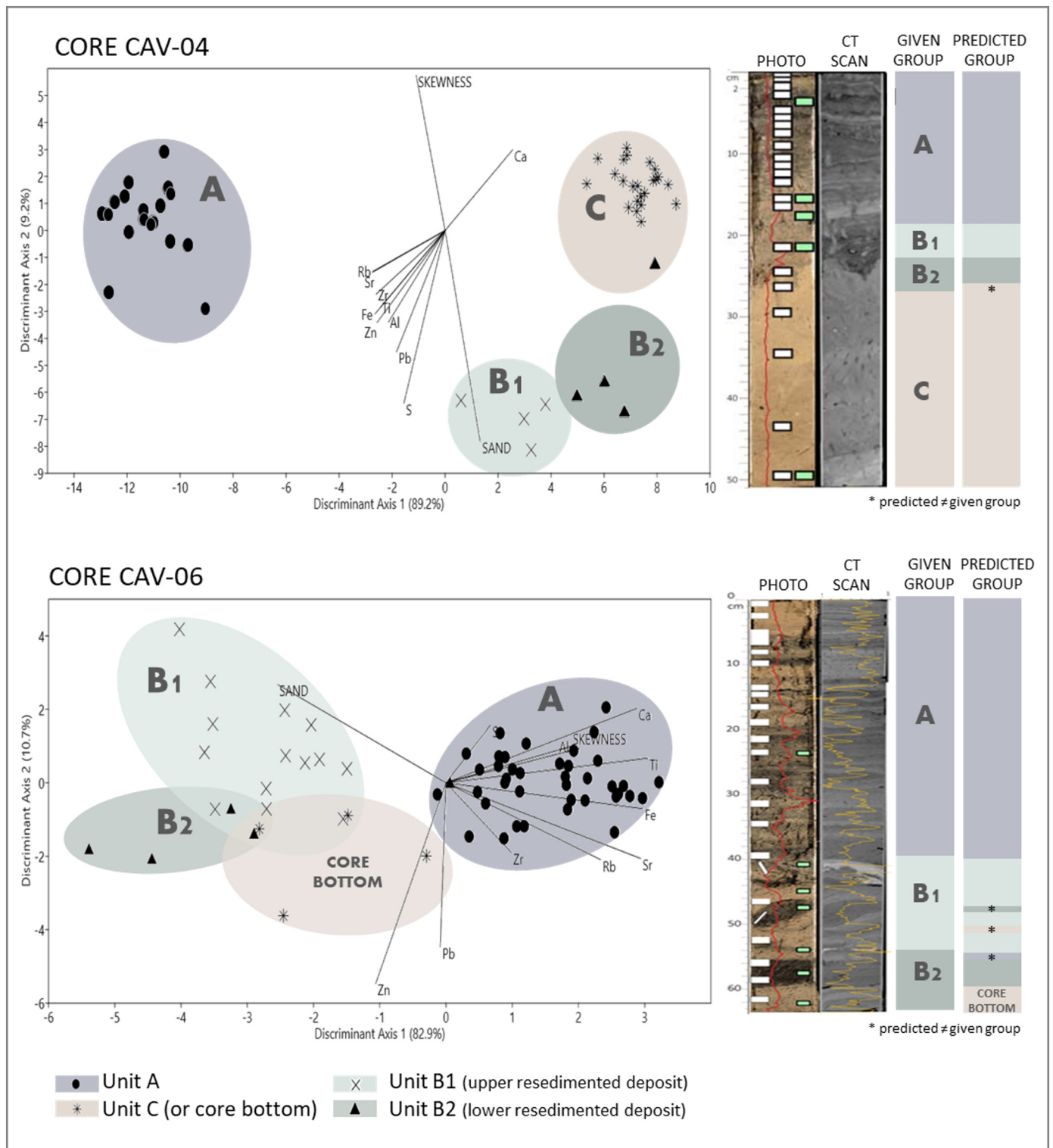
Fig. 7. Biplot of scores from the linear discriminant analysis (LDA) for the cores CAV-04 and CAV-06. The eigenvalue shows the explained relative variance for each discriminant function (axis). Points are 1 cm vertical resolution samples grouped by symbols ("a priori" classification — given groups) and colours (a posteriori classification — predicted groups).

geochemical composition. The Unit A in the CAV-04 is positively correlated to the increase of all element level, except for Ca. On the other hand, Ca is the element that better explains Unit C (which presents the lowest overall element level), while S has more importance in the Subunits B1 and B2. The Kruskal Wallis comparison test for each geochemical and granulometric variable among the sediment units classified "a posteriori" are provided as supplementary material (Figs. DIB16 and DIB17 Polonia et al., 2021).

The sand content and skewness (Ska) are sedimentological properties that also discriminate Unit A from Units B and C in the core CAV-04 (Fig. DIB18 Polonia et al., 2021). The Ska was computed as a statistical measure of grain size distribution from the Method of Moments (Arithmetic — μm). The Unit A has the lowest percentage of sand and is positively skewed (contribution of coarser sediments). In turn, Subunits B1 and B2 have higher sand content and are more negatively skewed, with very similar granulometric characteristics.

Unit C has an intermediate average sand content, and a symmetrical grain size distribution curve.

The statistical discrimination of Units A and B in the core CAV-06 is also evident, while the bottom of this core has transitional characteristics suggesting it contains sediments close to Unit C (Fig. 7). An input of coarser grains is also notable in Unit B, which increases the average sand content and makes the grain size distribution more positively asymmetrical (Fig. DIB18 Polonia et al., 2021). However, differently from what is observed in CAV-04, both Subunit B are not much coarser than Units A and C. The Subunit B2 is discriminated from B1 by the enrichment in Zn, Pb, and Zr.

As the two first discriminant axes are correlated to the carbon and nitrogen geochemical data (variables not considered in the matrix input for LDA), the results from the discriminant functions were used as indirect measure of the compositional features of the sediment layers. The analysis of the correlation matrix presented in the Fig. DIB19 (Polonia et al., 2021), in particular, allows to highlight the importance of the higher concentrations of inorganic carbon and C/N ratio for the Unit C in CAV-04.

4. Discussion

The combined interpretation of seismic reflection profiles and multi-proxy analysis of sediment samples was used to reconstruct stratigraphy, sediment deformation and environmental changes. Sediment colour changes, grain-size, and distribution of accessory elements, suggest a subdivision of the most recent lacustrine sedimentary record into three main units. While Units A and C appear to be in situ, Unit B is resedimented by a high-energy process during a sudden event in the lake basin.

The topmost Unit A was deposited under the present-day conditions, and correlates well between all cores, showing similar lithology and sedimentological properties, although being characterized by different thickness and accessory elements (Figs. 4–5). Lacustrine sedimentation in Unit A is represented in all cores by well-laminated sediments, with sub-horizontal, alternating light and dark levels. The mm-scaled sub-horizontal laminae, mostly visible in CAV-03 and CAV-06, suggests low energy sedimentary processes, probably due to seasonal variations and are tentatively interpreted as varves.

Unit B, shows a marked change in grain size and sediment structure among the cores, with sand reaching up to 66%. In CAV-06, Unit B is thicker, and shows a complex character related to the presence of deformed layers with different composition and grain size, suggesting multiple sediment stacks. We identify two main Subunits (B1 and B2) with two very reflective layers on CT scan images marking their top. XRD analyses, performed on the thickest highly-reflective layers, suggest they are made of 50–60% of calcite, more than twice the background value (Table DIB8 Polonia et al., 2021). Because of the coarse grain size, the carbonate is likely of detrital origin. This is supported by SEM and BSE images, which show angular grains of calcite and dolomite. The likely source areas for the detrital carbonate are located in the Mesozoic rocks surrounding the lake. Unit B in CAV-06 is clearly suggestive of a high-energy process, as indicated by the presence of inclined/deformed layers, abundant wood particles, and coarser grain size. In core CAV-04, Unit B is massive, and marked by an erosional basal scour. Similar to core CAV-06, two distinct sand peaks allow identifying Subunits B1 and B2 in this core. All these observations led us to conclude that Unit B should be related to remobilization of sediments triggered by an instantaneous event capable to bring sand from near-shore deposits or the catchment to the lake centre. Combined $\delta^{18}O/\delta^{13}C$ variability of carbonates and absolute ranges are similar with those published for southern-alpine Mesozoic to Cenozoic carbonates (e.g., Tanner, 2010) and compatible with a detrital sediment source. Isotopic signals do not indicate an authigenic mineral precipitation in the lake and in particular carbon isotopes can be reconciled with a marine composition and there is no evidence for methanogenetic carbonate precipitation.

With a meteoric $\delta^{18}O$ signal in the precipitation of −9 to −12‰ V-SMOW in the region (Giustini et al., 2016) and the ambient temperatures of lake water, the oxygen isotope signature of endogenic deep lake calcites would be expected to be around 5‰ lower than that observed from the detrital material here. The repeated $\delta^{18}O_{carb}$-increase in bulk lake sediments over the expected endogenic calcite signal, results predominantly from the quantity of introduced detrital grains from eroded marine carbonates, and has been used as a paleoflood proxy in the Austrian lake Mondsee (Kämpf et al., 2020).

Unit C was sampled only in core CAV-04, at shallower locations under the lower deposition rate conditions. It appears rather homogenous in colour and grain size, without major sedimentary structures.

Radiometric data combined with varve counting suggest that Unit B was deposited during the 1970's, under anthropogenic (power plant and viaduct constructions) and natural (river flood and two seismic events) stressors. In this reconstruction, Unit A post-dates the construction of the power plant, while Unit C should represent the pristine lacustrine environment. In the following sections, we will analyze how the lake sediments have recorded the expected environmental changes, and which could be the triggering mechanism for the deposition of resedimented Unit B.

4.1. Unit A and the anthropogenic stressor on lake ecosystem

After 1958, the emplacement of the *Somplago* power-plant led to a connection between the lake and the high-altitude *Ambiesta* water bodies, with inflows of cold waters and sediments from a different catchment area. The artificial water inflow led to temperatures 6 to 7 °C lower in summer (Pironio, 1989). Another consequence of the power plant and the construction of an artificial outflow was a reduction of the lake extension, from the original 1.74 km² to about 1.2 km², causing the exposure of a wide alluvial plain along the northern and the southern shores (Pironio, 1989).

Unit C pre-dates the *Somplago* power-plant construction. It was deposited when the lake was an isolated basin. It is rich in calcite and dolomite, in agreement with the mostly Triassic-Cretaceous limestones and dolostones outcropping around its shores. On the contrary, Unit A is low in calcite and dolomite, low in Ca in the XRF data and in CaCO₃, low in inorganic C and shows an increase in mica and gypsum (Fig. DIB8 Polonia et al., 2021) in agreement with lithologies outcropping in the catchment area of the Ambiesta basin, which was connected to the lake in the course of the power plant construction (Venturini et al., 2009). This suggests that an abrupt variation in sediment composition marks the differences between Units A and C with an increased input of fine-grained deposits within Unit A (Fig. 4). Unit A shows also sedimentological characteristics very different from lowermost Unit C, where no lamination is present. In our interpretation, the uppermost black and white laminae are seasonal, and occur only in Unit A and might thus be related either to increased input of cold waters or eutrophication possibly related to higher nutrient inflows leading to seasonally anoxic conditions at the lake bottom. Geochemistry of Unit A, in fact, shows that dark laminae are characterized by higher levels of S, Sr, TOC, and more negative $\delta^{13}C_{org}$, possibly indicating more reducing condition due to mild eutrophication (Hollander and Smith, 2001). However, since the S enrichment is associated with the presence of gypsum from the artificial catchment region (the analysed dark lamina has three times higher concentrations in gypsum relative to the light laminae, Fig. DIB8 Polonia et al., 2021) it is likely that the S-rich and reducing conditions are related to the input of water from the power plant starting from the time of its emplacement. Statistical analyses of XRF data within Unit A show different clusters with similar characteristics (Fig. DIB21 Polonia et al., 2021). Cluster 1 is characterized by higher values of Si/Al (aluminosilicates/biogenic silica), Ca/Al (calcium carbonate), Ba/Al (productivity), S/Al (bottom water anoxia/gypsum), suggesting stronger influence of sediments from the hydroelectrical power plant whose catchment area is rich in mica, evaporites and gypsum.

There is a partial concordance in the distribution of this group through the Unit A and the occurrence of dark laminae. The samples joined in Cluster 2 present intermediary geochemical characteristics and are distributed throughout the entire Unit A. Cluster 3 is characterized by higher values of Fe, Ti and Zr and there is some concordance in the distribution of this group and the "light brown" laminae occurrence in the upper portion of the Unit A. Other observations suggest a change in the sedimentation processes during 1990's such as varve thickness, which are thicker during 1970's and 1990's in the upper part of Unit A (Fig. 6). These variations and the geochemical characteristics of Cluster 3 could indicate climate driven changes in depositional processes and/ or anthropogenic triggers. Since the rainfall data (Fig. DIB13 Polonia et al., 2021) do not show significant changes during the 1990's we suggest that an anthropogenic stressor such as, for example, management of the water input by Somplago due to legal/environmental control or changes in the energy demand, is more likely.

Unit A also shows a relative enrichment in Zn and Pb since the early 1950s (Fig. 6a) that can be associated to the construction of the motorway close to the lake's shores and the likely additional inputs from the Somplago hydroelectric power plant. Similar trends were found in Lake Bled, a subalpine lake in Julian Alps in the NW part of Slovenia, mostly subjected to local pollution sources including traffic, sewage and agriculture (Ogorelec et al., 2006). Indeed, anthropogenic sources of Zn and Pb are generally linked to traffic, vehicle emissions and industrial activities (Romano et al., 2012; Nazarpour et al., 2019). However, XRF measurements are semi-quantitative and cannot provide reliable concentrations that can be compared with Sediment Quality Guidelines (SGQs) developed to define the state of contamination by assessing a probability for the occurrence of adverse biological effects in organisms due to their interaction with contaminants (MacDonald et al., MacDonald et al., 2000).

Only core CAV-04 did penetrate into the sediment to sample pristine lacustrine environment, i.e., before the 1950's, and the lack of radiometric data in Unit C does not allow to verify directly whether sedimentation rate varied after the power plant construction. However, ^{137}Cs indicates a sedimentation rate of 0.35–0.7 cm yr^{-1} during the last decades. If we assume these rates as stable in time and representative of the whole basin, they suggest an averaged sedimentation rate of 5 m ka^{-1}. Seismic reflection profiles in the southern sediment wedge show a major unconformity at about 10–15 m below the lake floor (Fig. 3c), which constitutes the base of a thick well-layered, plain-parallel sequence. Although in absence of direct sampling and dating, we might assume that these sediments started to accumulate after the LGM (about 10 ka) above an erosional unconformity which should mark the retreat and establishment of lacustrine conditions. 10 to 15 m of Holocene lacustrine sediments (about 10 ka) would imply a natural sedimentation rate much lower than that characterizing the lacustrine environment after the 1950's. Enhanced sediment influx after the construction of the hydropower plant in 1958 (Garzon, 2011) might thus have produced a sedimentation rate about 3–5 times higher than pristine conditions. Implications of these results are multiple.

The water and sediment discharges from the hydroelectric power plant modified the quality of the environment and decreased water temperatures as reported by local populations. Clastic sediments from different catchment areas are collected in the lake basin which constitutes an effective sediment trap. This has limited the delivery of sediments to the surrounding alluvial plains and coastal areas. Evaluating *ex post* the effects of artificial modification in a natural environment such as the Cavazzo lake during relatively long-time spans (decades) can provide important insights for managing and protection of similar environments worldwide. Major changes on the lake of Cavazzo ecosystem during the last decades may be summarized in two points. 1) The sedimentation rate in the lake after the power-plant construction increased by about 3–5 times; however, the final fate of these sediments would have been supplying alluvial plains and coastlines along the Adriatic coast, which suffer beach erosion; this leads to a further

unbalance between sediment deposition vs. subsidence and erosion, which require periodic and expensive interventions. 2) The construction of the power plant marks an abrupt change in the sediment mineralogy and geochemistry, and a relative increase in S, Pb, Zn, corresponding to the establishment of alternating reducing conditions at the lake floor not observed before.

Our results suggest that the major impact on the lake environment since 1950's is the increased sediment discharge and its changed geochemical character, which was found associated with reducing conditions at the lake floor and a relatively increased input of heavy metals. These effects should be taken into account when implementing watershed management practices since they regulate the short-term responses to anthropogenic and natural stressors. An approach that takes into account multiscale spatial and temporal linkages to all variables, as well as effective monitoring of environmental conditions is required. Investigating individual and combined stressors' effects can lead to a more comprehensive analysis of the risk and trade-offs in every managerial decision that will enable an efficient use of resources.

4.2. Is Unit B a lacustrine seismo-turbidite?

Unit B's composition and structure call for anomalous sedimentary processes whose triggering mechanism was capable of producing sediment remobilization both at the lake margins (CAV-04) and close to its depocenter (CAV-06). Several hints for sediment reworking by high-energy processes are present in this unit, such as coarser grain sizes, relatively large wood fragments, broken gastropods and ostracod remains, as well as displaced macrophyte-derived carbonate fragments. The construction of the viaduct (during 1970's) probably cannot be considered responsible of such processes because it may have impacted on the lake ecosystem but only locally, in the vicinity of the infrastructure, and is hardly considered responsible for deposition of relatively thick sand beds in the depocenter.

The construction of the power plant, on the other hand, is associated with massive excavation for the artificial outflow in the south. For this reason, we cannot exclude an anthropogenic impact especially considering the lake-level lowering during power plant construction that could have evoked slope instabilities and slumping. The slump deposit present at the toe of the sedimentary wedge in Fig. 3C, for example, may have been triggered by the construction of the Somplago power plant and lake-level lowering which probably caused slope instabilities and gravitational movements such as those described in the lake.

Other triggering mechanisms capable of producing the almost ubiquitous changes in sedimentation within Unit B are the massive 1966 Tagliamento river flood and the 1976/1977 Friuli earthquake sequence. Considering that the 1966 river flood did produce strong effects along the Tagliamento river valley but not in the lacustrine basin itself, we propose that seismic shaking during the 1976 seismic sequence is the best candidate for the deposition of the resedimented Unit B, also considering the sedimentological, geochemical and mineralogical observations that follow.

The earthquakes caused strong ground shaking and ubiquitous landslides in the whole area (Govi, 1977). Available data on co-seismic ground shaking (Tab. DIB22 Polonia et al., 2021) were recorded by the accelerometer installed at the Ambiesta dam (station TLM1, installed in 1973 in Tab. DIB22 Polonia et al., 2021) at about 10 km distance from the lake, and the SMU station, installed at the Somplago power-station after the May 6, 1976 event (http://itaca.mi.ingv.it/, n.d.; Fig. DIB23 Polonia et al., 2021). Our results suggest that the predicted PGA in the lake basin were in the range 50–236 cm/s^2, 49–231 cm/s^2 and 52–244 cm/s^2 during the May 6, and September 15, 1976 earthquakes respectively. Was seismic shaking strong enough to trigger slope failures and mass flows in the lake? Slope stability back calculations during two earthquakes in the lake Lucerne (Strasser et al., 2007) suggest that PGA above values of 78–137 cm/s^2 are capable to trigger mass movements in the lacustrine basin. In our case, the main event of May 6, 1976

and both September 15 events, are good candidates to trigger mass movements.

The study of slope instabilities performed through field observations and aerial photographic image interpretation (Govi, 1977) allowed to map a number of different landslides triggered by seismic shaking during the 1976 events close to the lake of Cavazzo. The Subunits B1 and B2, within Unit B, might thus represent lacustrine seismo-turbidite deposits (Moernaut et al., 2014) recording two events that have occurred some

months apart. Each of the two Subunits is topped by a calcitic mm- or cm-thick layer, deposited on top of a resedimented bed, characterized by in situ sediment deformation. If our reconstruction is correct, the two sandy layers, topped by detrital carbonate grains, suggest that major earthquakes during the Friuli 1976–77 seismic sequence might have produced remobilization of sediments in the lacustrine basin. In particular, the observation of larger thickness of the uppermost Ca-rich layer (on top of Subunit B1), combined with radiometric dating
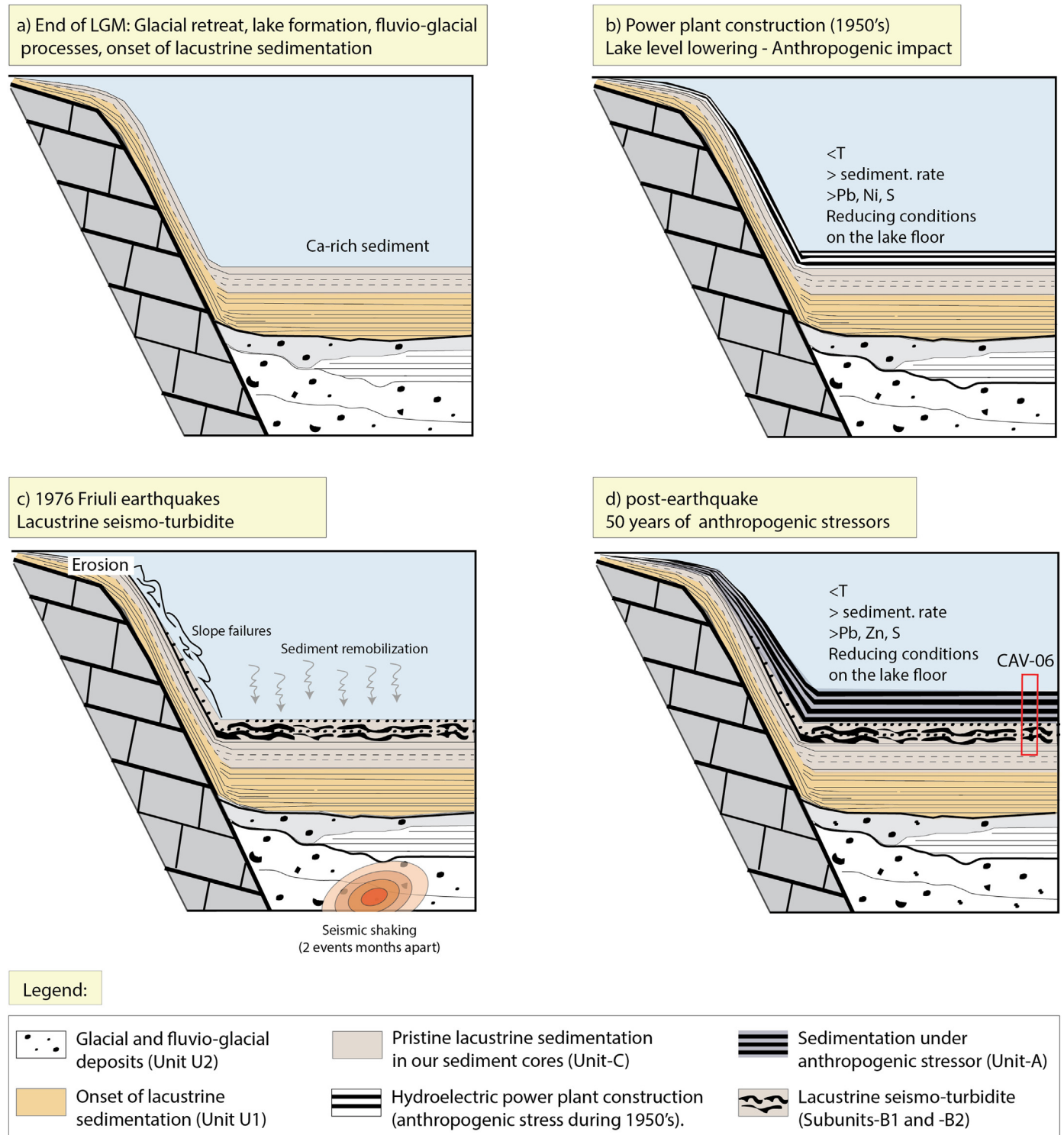

a) End of LGM: Glacial retreat, lake formation, fluvio-glacial processes, onset of lacustrine sedimentation

Ca-rich sediment

b) Power plant construction (1950's) Lake level lowering - Anthropogenic impact

<T
> sediment. rate
>Pb, Ni, S
Reducing conditions
on the lake floor

c) 1976 Friuli earthquakes Lacustrine seismo-turbidite

Erosion

Slope failures

Sediment remobilization

Seismic shaking
(2 events months apart)

d) post-earthquake 50 years of anthropogenic stressors

<T
> sediment. rate
>Pb, Zn, S
Reducing conditions
on the lake floor

CAV-06

Legend:

Glacial and fluvio-glacial deposits (Unit U2)

Onset of lacustrine sedimentation (Unit U1)

Pristine lacustrine sedimentation in our sediment cores (Unit-C)

Hydroelectric power plant construction (anthropogenic stress during 1950's).

Sedimentation under anthropogenic stressor (Unit-A)

Lacustrine seismo-turbidite (Subunits-B1 and -B2)

Fig. 8. Schematic diagrams and conceptual depositional model showing a) onset of lacustrine deposition during the Holocene; b) effects of hydroelectric power plant construction at the end of 1950's causing intermittent reducing conditions on the lake floor; c) co-seismic sedimentation during the 1976 Friuli earthquakes (in situ deformation and turbidity current involving carbonate grains); d) post 1976 sedimentation under anthropogenic stressors.

suggests a more intense sediment input during the most recent seismo-turbidite B1 emplacement, in agreement with seismological data suggesting that the September 15, 1976 earthquake was associated with the strongest PGA in the study region (Tab. DIB22 Polonia et al., 2021). Alternatively, we cannot exclude that the basal B2 Subunit is related to the power plant construction and Subunit B1 to the 1976 seismic events.

The internal structure of Subunits B1 and B2 in core CAV-06 suggests that sediment instability involved light brown sediments very similar to those of Unit C but also dark sediments (Fig.6). Since the dark layers are related to the power plant activity being present only in Unit A, this means that the remobilization of dark layers of Unit B took place after the construction of the Somplago power plant (Fig. 8). This is in agreement with the seismic trigger for Unit B during the 1976 events (i.e., about twenty years after the construction of the Somplago power plant in 1958). The intermediate geochemical characters of Unit B (Fig. 4) between Units A and C suggest mixing of different sediments with former Unit A, which was probably eroded and deformed during the high-energy events. Radiometric dating and varve counting support this interpretation providing an emplacement age for Unit B immediately before 1977. The event-beds show the highest carbonate content and decreased matrix and accessory minerals. During an earthquake the sediment surface may lose much of its matrix due to the resettling of coarse grains and export of the fine material. Here, the strong increase of grain size along with the dominance of detrital calcite point to an import from shallower site via mass-transport (Fig. DIB11 Polonia et al., 2021). In core CAV-06 the carbonate-rich layers do not show a clear erosive underside (Fig. 5), which may be related to the slow-down of an eventual turbidite near the deepest point of the lake. Corresponding beds in core CAV-04 (Fig. 4) have a clear erosive base, indicative for mass-transport at shallower sites. It is likely that these mass-transport-beds are related to the 1976 earthquake(s).

5. Conclusion

This work reconstructs major changes in the natural environment of the small alpine lake of Cavazzo. After the 1950's the Somplago hydroelectric power plant uses the lacustrine basin as terminal discharge of waters and sediments collected from different sources at different altitudes, in a mostly artificial catchment system. These artificial water and sediment inflows, led to changes in water temperatures and sediment loads relative to those characterizing the lake since its formation, at the end of the *Last Glacial Maximum*.

The recent lacustrine sedimentary record shows three main units. While the topmost and lowermost Units A and C appear to be in situ, Unit B is a resedimented bed triggered by a high-energy process during a sudden change in the lake basin sediment dynamics. Sediment analyses suggest that:

- An average sedimentation rate of 0.35 cm y^{-1} characterizes the lake margins while sedimentation rate close to the depocenter increases to 0.75 cm y^{-1}. The sedimentation rate increased sensibly after the construction of the power plant.
- An abrupt change in the sediment mineralogy and geochemistry occurred after the 1950's. Sediments deposited after the power plant construction receive contribution from an additional source higher in Al, Ti, Fe, Sr, S, Zr, Zn and Pb relative to the Ca-rich source that originally formed in the pristine environment.
- Further effects of the power plant impact are: i) increased finer grain size sediment input; ii) less abundant inorganic carbon; iii) associated sedimentary processes favoured the occurrence of sediment lamination with seasonal light and dark laminae or eutrophication; and iv) presence of dark laminae higher in S suggesting more reducing conditions on the seafloor.
- Unit B represents a lacustrine seismo-turbidite probably emplaced during the May 6 and September 15, 1976 seismic events. The deposition of seismo-turbidites after each earthquake is marked by in situ

soft deformation followed by the emplacement of a thin turbidite bed mainly composed of carbonate sand grains due to an import via mass transport from a shallow site to the deep-basin.

We stress the need of further data acquisition to better address the triggering mechanism and emplacement age of the resedimented bed. With the available data we cannot exclude a contribution from the hydroelectric power plant construction on sediment remobilization. The acquisition of long sediment cores going backwards in time will allow to identify co-seismic sedimentary processes for historic and prehistoric times and provide proxies to discriminate between natural and anthropogenic stressors.

Declaration of competing interest

The authors declare that they have no known competing financial interests or personal relationships that could have appeared to influence the work reported in this paper.

References

Ambraseys, N.N., 1976. The Gemona di Friuli earthquake of 6 May 1976. In: Pichard, P., Ambraseys, N.N., Ziogas, G.N. (Eds.), UNESCO Restricted Technical Report RP/1975-76 2.222.3., Part 2, Paris, France.

Anderlini, L., Serpelloni, E., Tolomei, C., De Martini, P.M., Pezzo, G., Gualandi, A., Spada, G., 2020. New insights into active tectonics and seismogenic potential of the Italiano

Southern Alps from vertical geodetic velocities. Solid Earth 11, 1681–1698. https://doi.org/10.5194/se-11-1681-2020.

Aoudia, A., Saraò, A., Bukchin, B., Suhadolc, P., 2000. The 1976 Friuli (NE Italy) thrust faulting earthquake: a reappraisal 23 years later. Geophys. Res. Lett. 27, 573–576. https://doi.org/10.1029/1999GL011071.

Appleby, P.G., Oldfield, F., 1992. Applications of ^{210}Pb to sedimentation studies. In: Ivanovich, M., Harmon, R.S. (Eds.), Uranium-series Disequilibrium. Applications to Earth Marine and Environmental Sciences, 2nd ed. Oxford Science, Oxford, U.K., pp. 731–738.

Bellucci, L.G., Frignani, M., Cochran, J.K., Albertazzi, S., Zaggia, L., Cecconi, G., Hopkins, H., 2007. ^{210}Pb and ^{137}Cs as chronometers for salt marsh accretion in the Venice Lagoon — links to flooding frequency and climate change. J. Environ. Radioact. 97, 85–102.

Bellucci, L.G., Giuliani, S., Romano, S., Albertazzi, S., Mugnai, C., Frignani, M., 2012. An integrated approach to the assessment of pollutant delivery chronologies to impacted areas: Hg in the Augusta Bay (Italy). Environ. Sci. Technol. 46, 2040–2046.

Benantelli, F., Busatto, T., Comoglio, C., La Piana, G., Maio, G., Marconato, E., Pizzul, E., Salviati, S., Tommasella, M., Vezza, P., 2011. Progetto impianto idroelettrico di Somplago (UD). Risultati indagine conoscitiva preliminare. Politecnico di Torino, Università degli Studi di Trieste, Aquaprogram s.r.l.

Bjerregaard, P., Andersen, O., 2007. Ecotoxicology of metals: Sources, transport, and effects in the ecosystem. In: Nordberg, G., Fowler, B., Nordberg, M., Friberg, L. (Eds.), Handbook on the Toxicology of Metals. Academic Press, pp. 251–277.

Braun, M., Hubay, K., Magyari, E., Veres, D., Papp, I., Bálint, M., 2013. Using linear discriminant analysis (LDA) of bulk lake sediment geochemical data to reconstruct late glacial climate changes in the South Carpathian Mountains. Quat. Intl. 293, 114–122. https://doi.org/10.1016/j.quaint.2012.03.025.

Chapron, E., Beck, C., Pourchet, M., Deconinck, J.F., 1999. 1822 earthquake-triggered homogenite in Lake Le Bourget (NW Alps). Terra Nova 11, 86–92.

Dal Forno, G., Gasperini, L., 2009. ChirCor: a new tool for generating synthetic chirp-sonar seismograms. Comput. Geosci. 34, 103–114. https://doi.org/10.1016/j.cageo.2007.01.004.

Doig, R., 1986. A method for determining the frequency of large-magnitude earthquakes using lake sediments. Can. J. Earth Sci. 23, 930–937. https://doi.org/10.1139/e86-094.

Dudgeon, D., Artington, A.H., Gessner, M.O., Kawabata, Z., Knowler, D., Léveque, C., Naiman, R.J., Prieur-Richard, A.H., Soto, D., Stiassny, M.L.J., Sullivan, C., 2006. Freshwater biodiversity: importance, threats, status and conservation challenges. Biol. Rev. 81 (2), 163–182. https://doi.org/10.1017/S1464793105006950.

Fanetti, D., Anselmetti, F.S., Chapron, E., Sturm, M., Vezzoli, L., 2008. Megaturbidite deposits in the Holocene basin fill of lake Como (Southern Alps, Italy). Paleogeogr. Paleoclimatol. Paleoecol. 259, 323–340. https://doi.org/10.1016/j.palaeo.2007.10.014.

Garzon, F., 2011. Perizia di valutazione del progetto Edipower.

Gasperini, L., Stanghellini, G., 2009. SeisPrho: an interactive computer program for processing and interpretation of high-resolution seismic reflection profiles. Comput. Geosci. 35, 1497–1507. https://doi.org/10.1016/j.cageo.2008.04.014.

Gasperini, L., Marzocchi, A., Mazza, S., Miele, R., Meli, M., Najjar, H., Michetti, A.M., Polonia, A., 2020. Morphotectonics and late Quaternary seismic stratigraphy of Lake Garda (Northern Italy). Geomorphology 371, 107427.

Gasperini, L., Ligi, M., Stanghellini, G., 2021. Pseudo-3D techniques for analysis and interpretation of high-resolution marine seismic reflection data. Boll. Geof. Teor. Appl. in press.

Giustini, F., Brilli, M., Patera, A., 2016. Mapping oxygen stable isotopes of precipitation in Italy. J. Hydrol. Reg. Stud. 8, 162–181. https://doi.org/10.1016/j.ejrh.2016.04.001.

Govi, M., 1977. Photo-interpretation and mapping of the landslides triggered by the Friuli Earthquake (1976). Bull. Intl. Assoc. Eng. Geol. 15, 67–72. https://doi.org/10.1007/BF02592650.

Hammer, Ø., Harper, D.A.T., Ryan, P.D., 2001. PAST: Paleontological Statistics software package for education and data analysis. Palaeontol. Electr. 4 (1) 9pp.

Han, Q., Tong, R., Sun, W., Zhao, Y., Yu, J., Wang, G., Shrestha, S., Jin, Y., 2020. Anthropogenic influences on the water quality of the Baiyangdian Lake in North China over the last decade. Sci. Total Environ. 701, 134929. https://doi.org/10.1016/j.scitotenv.2019.134929.

Heino, J., Alahuhta, J., Bini, L.M., Cai, Y., Heiskanen, A.S., Hellsten, S., Kortelainen, P., Kotamäki, N., Tolonen, K.T., Vihervaara, P., Vilmi, A., Angeler, D.G., 2021. Lakes in the era of global change: moving beyond single-lake thinking in maintaining biodiversity and ecosystem services. Biol. Rev. 96, 89–106. https://doi.org/10.1111/brv.12647.

Henares, S., Donselaar, M.E., Bloemsma, M.R., Tjallingii, R., De Wijn, B., Weltje, G.J., 2019. Quantitative integration of sedimentological core descriptions and petrophysical data using high-resolution XRF core scans. Mar. Petrol. Geol. 110, 450–462. https://doi.org/10.1016/j.marpetgeo.2019.07.034.

Henderson, P.A., 2002. Freshwater Ostracods. Pisces Conservation Ltd., Lymington and Pennington.

Hennekam, R., De Lange, G., 2012. X-ray fluorescence core scanning of wet marine sediments: methods to improve quality and reproducibility of high-resolution paleoenvironmental records. Limnol. Oceanogr. Methods https://doi.org/10.4319/lom.2012.10.991.

Hollander, D.J., Smith, M.A., 2001. Microbially mediated carbon cycling as a control on the DELTA13C of sedimentary carbon in eutrophic Lake Mendota (USA): new models for interpreting isotopic excursions in the sedimentary record. Geochim. Cosmochim. Acta 65 (23), 4321–4337. https://doi.org/10.1016/S0016-7037(00)00506-8.

Huang, J.-J., Löwemark, L., Chang, Q., Lin, T.-Y., Chen, H.-F., Song, S.-R., Wei, K.-Y., 2016. Choosing optimal exposure times for XRF core-scanning: suggestions based on the analysis of geological reference materials. Geochem. Geophys. Geosyst. 17, 1558–1566. https://doi.org/10.1002/2016GC006256.

Inouchi, Y., Kinugasa, Y., Kumon, F., Nakano, S., Yasumatsu, S., Shiki, T., 1996. Turbidites as records of intense palaeoearthquakes in Lake Biwa, Japan. Sediment. Geol., 104, pp. 117–125. doi:https://doi.org/10.1016/0037-0738(95)00124-7.

Kämpf, L., Plessen, B., Lauterbach, S., Nantke, C., Meyer, H., Chapligin, B., Brauer, A., 2020. Stable oxygen isotopes of carbonates in lake sediments as paleoflood proxy. Geology 48, 3–7. https://doi.org/10.1130/G46593.1.

MacDonald, D.D., Ingersoll, C.G., Berger, T.A., 2000. Development and evaluation of consensus-based sediment quality guidelines for freshwater ecosystems. Arch. Environ. Contam. Toxicol. 39, 20–31.

Malika, C., Ghazzali, N., Boiteau, V., Niknafs, A., 2014. NbClust: an R package for determining the relevant number of clusters in a data set. J. Stat. Softw. 61, 1–36. http://www.jstatsoft.org/v61/i06/paper.

Martinis, B., Cavallin, A., 1978. Ground cracks caused by the Friuli earthquake, 1976 from M. Cuarnan and Tremugna valley. Proceedings Spec. Meet. on the 1976 Friuli Earthquake and the Antiseismic Design of Nuclear Installation, CNEN, Roma, pp. 87–102.

Moernaut, J., 2020. Time-dependent recurrence of strong earthquake shaking near plate boundaries: a lake sediment perspective. Earth-Sci. Rev. 210 (November 2020), 103344. https://doi.org/10.1016/j.earscirev.2020.103344.

Moernaut, J., Daele, M.V., Heirman, K., Fontijn, K., Strasser, M., Pino, M., Urrutia, R., De Batist, M., 2014. Lacustrine turbidites as a tool for quantitative earthquake reconstruction: new evidence for a variable rupture mode in south central Chile. J. Geophys. Res. Solid Earth 119, 1607–1633. https://doi.org/10.1002/2013JB010738.

Monegato, G., Stefani, C., 2011. Preservation of a long-lived fluvial system in a mountain chain: the Tagliamento Valley (southeastern Italian Alps). In: Davidson, S.K., Leleu, S., North, C.P. (Eds.), From River to Rock Record: The Preservation of Fluvial Sediments and their Subsequent Interpretation. SEPM Spec. Publ. 97, pp. 359–374. https://doi.org/10.2110/sepmsp.097.359.

Nazarpour, A., Watts, M.J., Madhani, A., Elahi, S., 2019. Source, spatial distribution and pollution assessment of Pb, Zn, Cu, and Pb isotopes in urban soils of Ahvaz City, a semi-arid metropolis in southwest Iran. Sci. Rep. 9.

Ogorelec, B., Bole, B., Leonidakis, J., Cermelj, B., Mišič, M., Faganeli, J., 2006. Recent sediment of Lake Bled (NW Slovenia): sedimentological and geochemical properties. In: Kronvang, B., Faganeli, J., Ogrinc, N. (Eds.), The Interactions Between Sediments and Water. Springer, Dordrecht https://doi.org/10.1007/978-1-4020-5478-5_15.

Peruzza, L., Poli, M.E., Rebez, A., Renner, G., Rogledi, S., Slejko, D., Zanferrari, A., 2002. The 1976–1977 seismic sequence in Friuli: new seismotectonic aspects. Mem. Soc. Geol. It. 57, 391–400.

Pieri, V., Martens, K., Stoch, F., Rossetti, G., 2009. Distribution and ecology of non-marine ostracods (Crustacea, Ostracoda) from Friuli Venezia Giulia (NE Italy). J. Limnol. 68 (1), 1–15.

Pironio, P., Dri, G., Rabassi, V., 1989. Condizioni fisiche del lago di Cavazzo o dei Tre Comuni. (a cura di). Obiettivo lago. Il lago di Cavazzo o dei Tre Comuni: un patrimonio da salvare e valorizzare. Atti del Convegno Tecnico Scientifico, Alesso di Trasaghis 12–13 Settembre 1987, Treu Arti Grafiche, Tolmezzo.

Poli, M.E., Peruzza, L., Rebez, A., Renner, G., Slejko, D., Zanferrari, A., 2002. New seismotectonic evidence from the analysis of the 1976–1977 and 1977–1999 seismicity in Friuli (NE Italy). Boll. Geof. Teor. Appl. 43 (1–2), 53–78.

Polonia, A., Albertazzi, S., Bellucci, L.-G., Bonetti, C., Bonetti, J., Gallerani, A., Giorgetti, G., Giuliani, S., Lopez Correa, M., Mayr, C., Miserocchi, S., Peruzza, L., Savelli, F., Stanghellini, G., Gasperini, L., 2021. Multidisciplinary dataset for geological and environmental studies in the lake of Cavazzo (Southern Alps). Data Brief Submitted.

Pondrelli, S., Ekström, G., Morelli, A., 2001. Seismotectonic re-evaluation of the 1976 Friuli, Italy, seismic sequence. J. Seismol. 5, 73–83. https://doi.org/10.1023/A:1009822018837.

R Core Team, 2020. R: A Language and Environment for Statistical Computing. R Foundation for Statistical Computing, Vienna, Austria URL http://www.R-project.org/.

Richter, T.O., Van der Gaast, S., Koster, B., Vaars, A., Gieles, R., de Stigter, H.C., de Haas, H., van Weering, T.C.E., 2006. The Avaatech XRF Core Scanner: technical description and applications to NE Atlantic sediments. Geol. Soc. Lond. Spec. Publ. 267 (1), 39–50. https://doi.org/10.1144/GSL.SP.2006.267.01.03.

Romano, S., Mugnai, C., Giuliani, S., Turetta, C., Cu, N.H., Bellucci, L.G., Nhon, D.H., Capodaglio, G., Frignani, M., 2012. Metals in sediment cores from nine coastal lagoons in central Vietnam. Am. J. Environ. Sci. 8, 130–142.

Rovida, A., Locati, M., Camassi, R., Lolli, B., Gasperini, P., 2020. The Italian earthquake catalogue CPTI15. Bull. Earth. Eng 18 (7), 2953–2984. https://doi.org/10.1007/s10518-020-00818-y.

Saber, A., James, D.E., Hannoun, I.A., 2020. Effects of lake water level fluctuation due to drought and extreme winter precipitation on mixing and water quality of an alpine lake, case study: Lake Arrowhead, California. Sci. Total Environ. 714, 136762. https://doi.org/10.1016/j.scitotenv.2020.136762.

Sandron, D., Renner, G., Rebez, A., Slejko, D., 2014. Early instrumental seismicity recorded in the eastern Alps. Boll. Geof. Teor. Appl. 55 (4), 755–788. https://doi.org/10.4430/bgta0118.

Saraò, A., Sugan, M., Bressan, G., Renner, G., Restivo, A., 2021. A focal mechanism catalogue of earthquakes that occurred in the southeastern Alps and surrounding areas from 1928–2019. Earth Syst. Sci. Data Discuss. https://doi.org/10.5194/essd-2020-369 [preprint]. in review.

Simmoneau, A., Chapron, E., Vanniere, B., Wirth, S.B., Gilli, A., Di Giovanni, C., Anselmetti, F.S., Desmet, M., Magny, M., 2013. Mass-movement and flood-induced deposits in Lake Ledro, southern Alps, Italy: implications for Holocene palaeohydrology and natural hazards. Clim. Past 9, 1–16. https://doi.org/10.5194/cp-9-1-2013. www.clim-past.net/9/1/2013/.

Sims, J.D., 1975. Determining earthquake recurrence intervals from deformational structures in young lacustrine sediments. Tectonophysics 29 (1–4), 141–152. https://doi.org/10.1016/0040-1951(75)90139-0.

Slejko, D., Neri, G., Orozova, I., Renner, G., Wyss, M., 1999. Stress field in Friuli (NE Italy) from fault plane solutions of activity following the 1976 mainshock. Bull. Seism. Soc. Am. 89, 1037–1052.

Smol, J.P., 2019. Under the radar: long-term perspectives on ecological changes in lakes. Proc. R. Soc. B 286, 20190834. https://doi.org/10.1098/rspb.2019.0834.

Strasser, M., Anselmetti, F.S., Donat, F., Giardini, D., Schnellmann, M., 2006. Magnitudes and source areas of large prehistoric northern Alpine earthquakes revealed by slope failures in lakes. Geology 12, 1005–1008. https://doi.org/10.1130/G22784A.1.

Strasser, M., Stegmann, S., Bussmann, F., Anselmetti, F.S., Rick, B., Kopf, A., 2007. Quantifying subaqueous slope stability during seismic shaking: Lake Lucerne as model for ocean margins. Mar. Geol. 240 (1–4), 77–97. https://doi.org/10.1016/j.margeo.2007.02.016.

Suhadolc, P., 1981. Spatial distribution of the aftershock sequence relative to the September 16, 1977 Friuli earthquake. Boll. Geof. Teor. Appl. 23, 331–348.

Tanner, L.H., 2010. The Triassic isotope record. In: Lucas, S.G. (Ed.), The Triassic Timescale. Geological Society, London, Special Publications vol. 334, pp. 103–118. https://doi.org/10.1144/SP334.5.

Van Daele, M., Haeussler, P.J., Witter, R.C., Praet, N., De Batist, M., 2020. The sedimentary record of the 2018 Anchorage earthquake in Eklutna Lake, Alaska: calibrations the lacustrine seismograph. Seismol. Res. Lett. 91 (1), 126–141. https://doi.org/10.1785/0220190204.

Venturini, C., Discenza, K., 2010. Stratigrafia e paleo-idrografia del Friuli centrale (Prealpi Carniche) Miocene superiore-Pliocene inferiore. Gortania Udine 30 (VI), 31–52.

Venturini, C., Spalletta, C., Vai, G.B., Pondrelli, M., Fontana, C., Delzotto, S., Longo Salvador, G., Carulli, G.B., 2009. Note illustrative della Carta geologica d'Italia alla scala 1:50.000, Foglio 031 Ampezzo. ISPRA, Serv. Geol. It 232 pp.

Wentworth, C.K., 1922. A scale of grade and class terms for clastic sediments. J. Geol. 30, 377–392.

Zanferrari, A., Masetti, D., Monegato, G., Poli, M.E., 2013. Geological map and explanatory notes of the Italian Geological Map at the scale 1:50,000: Sheet 049 "Gemona del Friuli". ISPRA - Servizio Geologico d'Italia - Regione Autonoma Friuli Venezia Giulia 262 pp. http://www.isprambiente.gov.it/Media/carg/friuli.html.

Web-resources

http://itaca.mi.ingv.it/.
www.meteo.fvg.it.